NONLINEAR RESONANCE ULTRASONIC SPECTROSCOPY FOR CHARACTERIZING THERMAL DAMAGE IN 17-4PH STAINLESS STEEL

A Thesis
Presented to
The Academic Faculty

by

Marc Forstenhaeusler

In Partial Fulfillment
of the Requirements for the Degree
Master of Science in
Engineering Science and Mechanics

School of Civil and Environmental Engineering
Georgia Institute of Technology
December 2016

NONLINEAR RESONANCE ULTRASONIC SPECTROSCOPY FOR CHARACTERIZING THERMAL DAMAGE IN 17-4PH STAINLESS STEEL

Approved by:

Professor Laurence J. Jacobs, Advisor
School of Civil and Environmental Engineering
Georgia Institute of Technology

Dr. Jin-Yeon Kim
School of Civil and Environmental Engineering
Georgia Institute of Technology

Dr. Jianmin Qu
G.W. Woodruff School of Mechanical Engineering
Georgia Institute of Technology

Date Approved: 26 August 2016

And yet it moves

Galileo Galilei

ACKNOWLEDGEMENTS

Throughout my research, I have been lucky to have the support of my advisors Prof. Laurence Jacobs and Dr. Jin-Yeon Kim. They provided a highly motivative atmosphere during my time at Georgia Tech. I want to thank Prof. Jacobs for always supporting me throughout my graduate studies, for the help regarding all kind of problems and for giving me the opportunity to take part in the Quantitative Non-destructive Evaluation conference in Atlanta. Furthermore, I want to thank Dr. Jin-Yeon Kim for his invaluable advice and help with experiments, discussions, and by sharing his experience in the field of non-destructive evaluation. Thanks goes to Dr. Jianmin Qu from Northwestern University for serving as a committee member and reviewing this thesis. I would like to express my special thanks to Professor Lothar Gaul, Professor Arnold Kistner and Christian Ehrlich from the University of Stuttgart for choosing me as a candidate for the ISAP Program, which is financially supported by the DAAD. The DAAD is gratefully acknowledged for supporting me with its scholarship. Thanks goes to my labmates Katie Scott, Gun Kim, David Torello, Mehdi Rashidi, Christoph Doerr and Daniel Gruen providing an engaging and motivating atmosphere in the lab. I want to thank Christoph Doerr and Daniel Gruen for sharing joy and sorrow with me during this year in Atlanta. Finally I want to thank all my friends and family back in Germany for their support.

TABLE OF CONTENTS

LIST OF TABLES

LIST OF FIGURES

SUMMARY

Nonlinear resonance ultrasonic spectroscopy (NRUS) has been widely used to determine the hysteretic nonlinearity parameter, α for mesoscopic elastic materials. The current research adopts the NRUS to characterize microscopic material damage in metallic specimens with small dimensions. The geometric limitations in these small samples greatly restrict applications of other nonlinear ultrasonic techniques such as the higher harmonic generation technique.

Two opposite edges of a rectangular plate specimen (10x10x2mm) are clamped by a specially designed fixture and an excitation piezoelectric transducer is attached to one of the other edges. The excitation transducer provides a frequency sweep around a resonance repsonse of the specimen while the out of plane velocity of the specimen is detected by a laser vibrometer.

To simulate the copper-rich precipitate (CRP) formation and the associated irradiation damage in reactor pressure vessel steels, thermally aged 17-4 PH stainless steel in different precipitation stages is used to study the effects of CRPs on the measured hysteretic nonlinearity parameter, α. These results are compared to propagating wave nonlinear ultrasonic technique results on larger specimens and it is shown that the NRUS method is quite sensitive to the microstructure changes due to copper precipitates in this material.

Nomenclature

Abbreviations

AC	Air cooled
BS	Beam splitter
D	Detector
EDM	Electrical discharge machining
FFT	Fast Fourier transformation
GQ	Gas quenched
NDE	Nondestructive evaluation
NRUS	Nonlinear resonant ultrasonic spectroscopy
PH	Precipitate-hardenable
PM	Priesach-Mayergoyz
RPV	Reactor pressure vessels
RUS	Resonance ultrasonic spectroscopy
TEP	Thermo-electric power
WQ	Water quenched

Formula Signs

Latin symbol	description
A	hysteretic term
A_1	amplitude first harmonic
A_2	amplitude second harmonic
$\vec{b}$	Burgers vector
b_j	body force
c_L	phase velocity of the longitudinal wave
c_S	phase velocity of the shear wave
C_{ijkl}	fourth order stiffness tensor
E	Young's modulus
$f(x,t)$	external force
f_{in}	input frequency
f_0	resonance frequency for a infinitesimal small amplitude
Δf	frequency shift
F_0	force amplitude
F_p	resisting force of a precipitate
$\tilde{F}(t)$	external force
K	bulk modulus
K_0	linear modulus
l_c	length closed
l_o	length open
L	bar length
L_N	breakaway length
L_p	precipitate distance
n_i	unit normal vector

Q	damping coefficient
r_p	radius of second phase particle
R	bowing radius, maximal strain
R^2	coefficient of determination
S	surface area
t	time
t_j	traction vector
T	line tension, period
u	displacement vector
$\ddot{u}$	acceleration
u_j	displacement
v	Poissons ratio, velocity
V	volume
x	Lagrangian coordinate
α	hysteretic nonlinearity parameter
α_E	longitudinal hysteretic nonlinearity parameter
α_G	torsional hysteretic nonlinearity parameter
β	nonlinearity parameter
γ	angle between the velocity vector and its normal component
δ	nonlinearity parameter
$\delta(x)$	delta function
δ_{ij}	Kronecker delta
ε	strain
ε_m	maximum strain
$\dot{\varepsilon}$	strain rate
ε_{kl}	strain tensor
$\Delta\varepsilon$	peak to peak strain

λ, μ	Lamé elastic constants
λ	wavelength laser
ρ	density
σ_A	classical nonlinear stress from lattice anharmonicity
σ_c	stress closed
σ_H	hysteretic nonlinear stress
$\sigma_i j$	Cauchy stress tensor
σ_o	stress open
τ	damping term
τ_c	critical shear stress
τ_d	shear stress
ϕ	bowing angle, phase
ϕ_c	critical bowing angle
Φ	scalar potential
Ψ	vector potential
ζ	angle between the incident and reflected beam
ω	driving frequency
ω_0	linear resonant frequency
Ω	relative frequency

CHAPTER I

INTRODUCTION

1.1 Motivation and Objective

Nondestructive evaluation (NDE) of materials is a growing field that has wide-reaching applications in a variety of areas including aerospace engineering (e.g., airplane wings and tails), civil engineering (e.g., bridges, buildings), and nuclear engineering (e.g., nuclear core reactor shields). Currently, structural safety is typically determined either by laboratory testing samples of the same material or conducting visual inspections. For example, for a concrete nuclear reactor shield, the same concrete mix will be poured into cylinder molds and, once cured, undergo compression and thermal testing. The longevity of the built shield will be extrapolated from the performance of these hopefully representative samples. In the case of bridges, the bridge material is tested, and the bridges are visually inspected on a calendar schedule. However, microcracks and other invisible damage occurs much earlier than damage that can be seen by human eyes, so these techniques do not allow us to detect damage at early stages, which could significantly reduce repairs costs and, in some cases, avert complete failure of built structures.

Ultrasonic detection methods are a standard in NDE because we know that the propagation of ultrasound depends on the elastic properties of the material. Linear ultrasonic NDE methods has become common practice in many industrial applications because it is very reliable and effective. Acoustic parameters of the propagating wave like the phase velocity, attenuation, transmission and reflection coefficients are measured to determine the elastic properties of a material. The elastic properties are changed if defects in the structure exist. Linear methods are capable of detecting

crack features on the order of the wavelength of the ultrasonic wave.

A complementary ultrasonic method is nonlinear ultrasonic NDE, which is sensitive to changes in the microstructure of a material that are orders of magnitude smaller than the wavelength. The changes in nonlinear ultrasonic features are generally much more sensitive to attributes of the microstructure than linear ultrasonic waves [26]. Therefore, nonlinear acoustic methods allow for the detection of microstructural features and damage at its earliest stages. The nonlinearity of a material is observable by: higher harmonic generation; sub-harmonic generation; a mixed frequency response or a shift in the resonance frequency [12][21].

The motivation for this current research is to detect radiation material degradation in reactor pressure vessels due to precipitates formation. Therefore, a nondestructive evaluation technique should be developed which is sensitive to this change in the microstructure. In previous research [20], it was experimentally shown that higher harmonic generation is sensitive to the presence of copper-rich precipitates in 17-4 PH stainless steel. The study in [20] used a transducer to emit a Rayleigh surface wave with frequency f_{in} into the specimen. A second air-coupled transducer receives the propagated Rayleigh wave signal. Due to the wave interaction with pinned dislocations, a second harmonic with frequency $2f_{in}$ can be detected [15]. The ratio of the second harmonic amplitude to the square of the primary harmonic amplitude is proportional to the acoustic nonlinearity parameter β, which is a measure of the material state of the sample analyzed [12][14].

The objective of this research is to develop a measurement procedure using the resonance frequency shift method, the nonlinear resonant ultrasonic spectroscopy (NRUS). In contrast to other research [30], the current work examines small (10mm x 10mm x 2mm) 17-4 PH stainless steel specimens. The geometric limitations in these small samples greatly restrict applications of propagating wave nonlinear ultrasonic techniques such as the higher harmonic generation technique.

First a robust, accurate experimental setting is developed which is capable of monitoring a shift in the resonance frequency depending on the excitation amplitude. Once this objective is achieved, in a second step the 17-4 PH stainless steel specimens at different precipitation stages, which have been used for the measurement of β, are examined to investigate the influence of small copper-rich precipitates in steel on the frequency shift occuring. Finally, the sensitivity of both methods are compared.

1.2 Structure of this Thesis

The first chapter provides a general introduction to the benefits and limitations of using nonlinear ultrasonic techniques to monitor microstructural changes due to radiation damage. An introduction into the fundamentals of wave propagation in solids, hysteretic based nonlinearity and a analytical solution for a resonant bar is given in chapter 2. Chapter 3 shows the experimental setup and provides different preliminary measurements to validate the accuracy of the setup. In the next chapter the material analyzed is described in particular the heat treatment and its actual state is shown. Chapter 5 presents the experimental results for different aging states and provides a discussion and interpretation of these results, in terms of previous microstructural characterizations. In the next chapter the measured results for nonlinearity parameter α are compared to the β-measurements and other complementary measurements. The final chapter provides a brief conclusion of the major results and provides recommendations for future work.

CHAPTER II

THEORETICAL BACKGROUND

2.1 Wave Propagation in Solids

The fundamentals of wave propagation in solids are summarized based on the statements of Achenbach [1].

In general for every elastic body which follows the laws of mechanics Newton's first law must be fulfilled for an arbitrary volume V covered by surface S, which can be written in tensor notation as

$$\int_S t_j \,\mathrm{d}A + \int_V \rho b_j \,\mathrm{d}V = \int_V \rho \ddot{u}_j \,\mathrm{d}V \,, \tag{1}$$

where ρ gives the density of the body, t_j is the traction acting on S, b_j the subjected body force and $\ddot{u}_j$ represents the second time derivative of the displacement u_j. The traction vector is defined by Cauchy's stress formula as the tensor product of unit vector n_i, normal to the surface t_j is acting on, and the Cauchy stress tensor σ_{ij}

$$t_j = \sigma_{ij} n_i \,. \tag{2}$$

Substitution of (2) into (1) yields

$$\int_S \sigma_{ij} n_i \,\mathrm{d}A + \int_V \rho b_j \,\mathrm{d}V = \int_V \rho \ddot{u}_j \,\mathrm{d}V \,, \tag{3}$$

which can be simplified by the divergence theorem

$$\int_S n_i \sigma_{ij} \,\mathrm{d}A = \int_V \sigma_{ij,i} \,\mathrm{d}V \tag{4}$$

to

$$\int_V (\sigma_{ij,i} + \rho b_j - \rho \ddot{u}_j) \,\mathrm{d}V = 0 \,. \tag{5}$$

Which is known as Cauchy's first law of motion in the form

$$\sigma_{ij,i} + \rho b_j - \rho \ddot{u}_j = 0\,, \tag{6}$$

which is valid for arbitrary small parts of the volume.

The stress-strain relation for an homogenous, isotropic, linear elastic solid is given by

$$\sigma_{ij} = C_{ijkl}\varepsilon_{kl}\,, \tag{7}$$

where σ_{ij} gives the stress, ε_{kl} the strain and C_{ijkl} the fourth order stiffness tensor. For homogenous, isotropic solids the stress strain relationship can be simplified to

$$\sigma_{ij} = \lambda \varepsilon_{kk}\delta_{ij} + 2\mu\varepsilon_{ij}\,. \tag{8}$$

using λ and μ known as the Lamé elastic constants. Expressed in terms of the Young's modulus E and the Poisson's ratio v

$$\lambda = \frac{Ev}{(1+v)(1-2v)} \qquad \mu = \frac{E}{2(1+v)}\,. \tag{9}$$

The strain ε in the linearized form of the strain-displacement relation is

$$\varepsilon_{ij} = \frac{u_{i,j} + u_{j,i}}{2}\,. \tag{10}$$

Substituting (8) and (10) in (6) and neglect body forces in tensorial notation yields

$$(\lambda + \mu)u_{i,ij} + \mu u_{j,ii} = \rho \ddot{u}_j\,, \tag{11}$$

which leads to the Navier elastodynamic equation, given in vector notation

$$\rho \ddot{u} = (\lambda + 2\mu)\nabla\nabla \cdot u - \mu \nabla^2 u\,. \tag{12}$$

Introducing the Helmholtz decomposition of the displacement vector u

$$u = \nabla\Phi + \nabla \times \Psi\,, \tag{13}$$

equation (12) can be solved in terms of the scalar potential Φ, which gives the compressional part of the displacement,

$$\nabla^2\Phi - \frac{1}{c_L^2}\ddot{\Phi} = 0\,, \tag{14}$$

and the vector potential Ψ, representing shear deformations and rigid rotations without volume change of the displacement,

$$\nabla^2\Psi - \frac{1}{c_S^2}\ddot{\Psi} = 0\,. \tag{15}$$

This leads to the phase velocities of the longitudinal wave c_L and the shear wave c_S given as

$$c_L = \sqrt{\frac{\lambda + 2\mu}{\rho}}\,, \tag{16}$$

and

$$c_S = \sqrt{\frac{\mu}{\rho}}\,. \tag{17}$$

After the linear case was discussed now the nonlinear case is considered. The wave equation (12) for nonlinear problem is expressed as a power series of the strain [8]

$$\frac{\partial^2 u}{\partial t^2} = \frac{K_0}{\rho}\frac{\partial}{\partial x}\left[\frac{\partial u}{\partial x} + \beta\left(\frac{\partial u}{\partial x}\right)^2 + \delta\left(\frac{\partial u}{\partial x}\right)^3 + \dots\right] + A[\varepsilon, \dot{\varepsilon}]\,, \tag{18}$$

where the first term on the right side equals the previously determined linear term in 1D extended by the nonlinear terms. These higher order nonlinear terms are part of the classical theory for nonlinear waves [16]. For example the β-term is known as the quadratic nonlinearity term and is used to determine the second harmonic generation in Chapter 4.

K_0 represents the linear modulus, which is the sum of the bulk modulus K and a constant term depending on the Lamé elastic constant μ

$$K_0 = K + \frac{4}{3}\mu\,, \tag{19}$$

therefore the linear modulus can be expressed in terms of Lamé elastic constants as

$$K_0 = \lambda + 2\mu\,. \tag{20}$$

In addition to these classical nonlinear terms a hysteretic term denoted by $A[\varepsilon, \dot{\varepsilon}]$ is added, and represents the contribution of hysteretic elastic elements as explained in section 2.2.

2.2 Hystertic Elastic Elements

Materials which exhibit classical nonlinear behavior include most fluids and monocrystalline solids; these materials belong to the "atomic-elasticity" class and have, because of their atomic lattice, a very homogeneous configuration. The nonlinearity in this class of materials is on the atomic scale and can be due to lattice anharmonicity, dislocations or microcracks. For example, dislocations and precipitates produce local atomic strain fields due to their geometrical deviation from the crystal structure. These strain fields are a nonlinear function and act as a source of nonlinear body forces, when a wave propagates through this localized disturbance.
In contrast to metals, concrete has a heterogeneous configuration and belongs to the "structural nonlinear elasticity" class [28]. For these types of materials, the nonlinearity is due to the mesoscopic structure. The mesoscopic structure of concrete consists of a hard matrix (grains, crystals) within which some softer features like cracks, voids, or interfaces between aggregate and the surrounding cementitious mortar are bonded. The nonlinear behavior of these materials is modeled by hysteretic elements.

In general material defects (e.g. cracks) weaken the stiffness of the structure, which in turn changes the resonance frequency of the system. Aside from the linear effect, some nonlinear response can be observed, due mostly to the presence of soft elements as discussed above. In [2],[4],[5] it was shown that not only mesoscopic structures show nonlinear effects that depend on the magnitude of applied strain and the corresponding time scale, like hysteresis or slow and nonlinear fast dynamics [13], but also similar effects were observed for material which belong to the "atomic-elasticity" class. Due to the anomalous nonlinear fast dynamics, the resonance frequency of

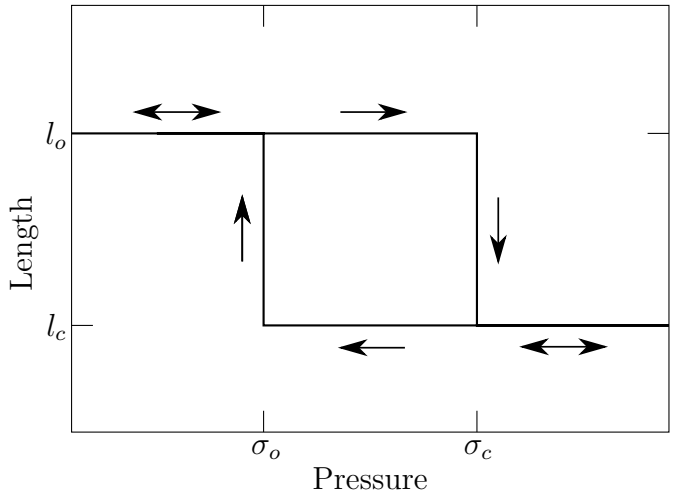

Figure 1: Hysteretic element

these materials changes proportionally to the excitation amplitude. For an increasing excitation amplitude, the resonance frequency is shifted to lower frequencies.

In [9] it is shown that the cause of nonlinearity can be attributed to the dynamic behavior of microcracks. The nonlinear behavior of this system is due to Hertzian contact of crack faces and/or opening and closing of cracks in response to exciting wave motion. The Priesach-Mayergoyz (PM) space model maps the hysteretic and discrete memory behavior. For this, the soft features (e.g. cracks) are modeled as hysteretic elastic elements, they behave like shown in Figure 1 [23] within two states. Each hysteretic elastic element, like a crack, has specific equations of state which contributes to the elasticity of the material. An element can be modeled as a feature whose length switches hysteretically between two states, open l_o and closed l_c, depending on the acting pressure (σ_o or σ_c). If an increasing stress is applied on an open element it jumps into the closed state as soon as it reaches σ_c and remains so. However, when the stress is decreased it changes back to length l_o when it reaches σ_o. Therefore, each element is defined by its specific set of parameters (l_o,l_c,σ_o,σ_c). We can think about a hysteretic elastic elements as a spring which switches instantly between two states, and enforces the two endpoints into its position l_o or l_c see Figure

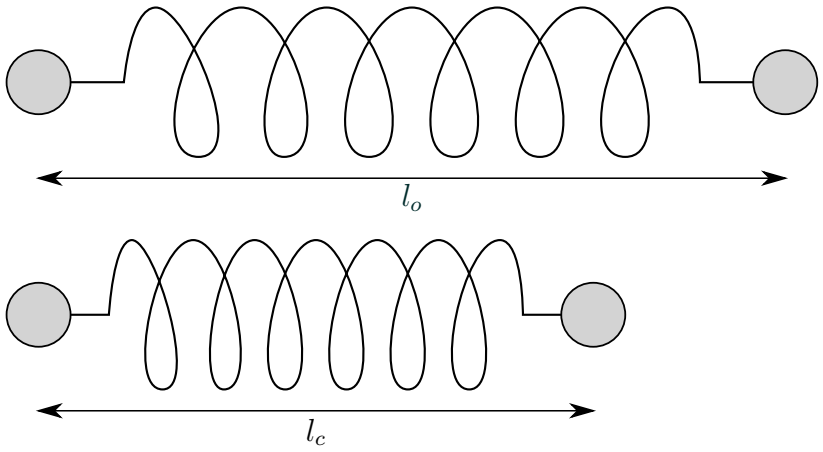

Figure 2: Two-state spring model, which switches instantly between two endpoints into its position l_o or l_c.

2. If we consider a stack of these hysteretic elastic elements depending on the pressure, some cracks can be open and some closed. In an extreme case for a high excitation the pressure is high enough, so that all crack faces stay in contact.

Guyer and Johnson [9] developed a model in which each elastic element is described by σ_o and σ_c as coordinates in the PM-space, see Figure 3. The y-axis gives opening stress σ_o and the x-axis the necessary stress that the hysteretic element closes again σ_c. If the stress is increased from $\sigma = 0$, representing the state where all elements are open, by passing σ_A to σ_B the corresponding strain is shown on the right site. The pictures on the bottom show the state of the elements for each stress level, closed hysteretic elements are black. So if the stress is increased more and more elements become closed, but if the stress decreases for example to A' some elements stay in the closed state because of their hysteretic behavior. This means the resulting strain is higher at the same stress level for a decreasing load than for an increasing. Which results in a hysteretic loop of the strain in the stress strain diagram. So, in general the strain of the system depends on the present stress as well as the stress history.

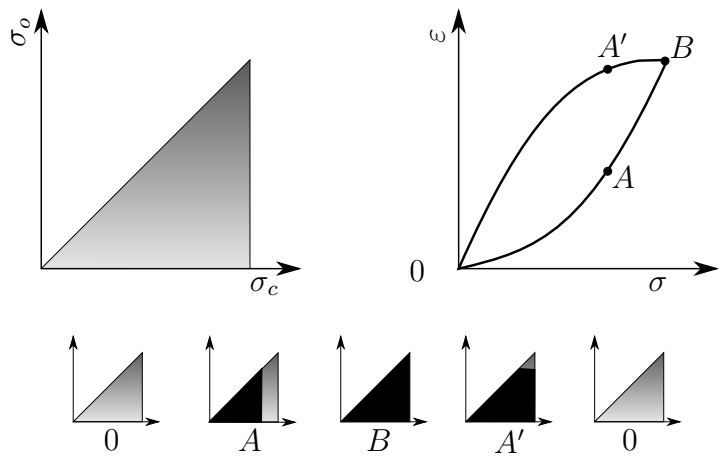

Figure 3: Stress protocol in Preisach space and the corresponding stress strain relation (simplified from [8]).

2.3 Precipitation Hardening and its Influence on the Microstructure

This section gives a brief introduction into general concepts of precipitates hardening and its interaction with dislocations; a detailed introduction to the concepts of precipitation hardening and their interaction with dislocations is given in [18].

Precipitation is a clustering process of solute atoms to form particles under appropriate thermal conditions. In general precipitation hardening occurs in alloys for which the solubility of the alloying element in the matrix material is temperature dependent. Only at high temperatures the alloying elements can fully dissolve in the matrix. If the solid solution is quenched very rapidly, there will not be sufficient time to adopt and a super saturated solid solution is obtained. Since the solubility of this alloying elements is low, by reheating for a sufficient time, the solute atoms start to diffuse and transform the microstructure towards the equilibrium state by loosing their free energy. An increase in hardness and therefore a greater resistance towards plastic deformation is observed after heat treatment.

The precipitation hardening can be split into three stages during the thermal aging of an alloy. In the first stage nucleation of many small precipitates of the solute

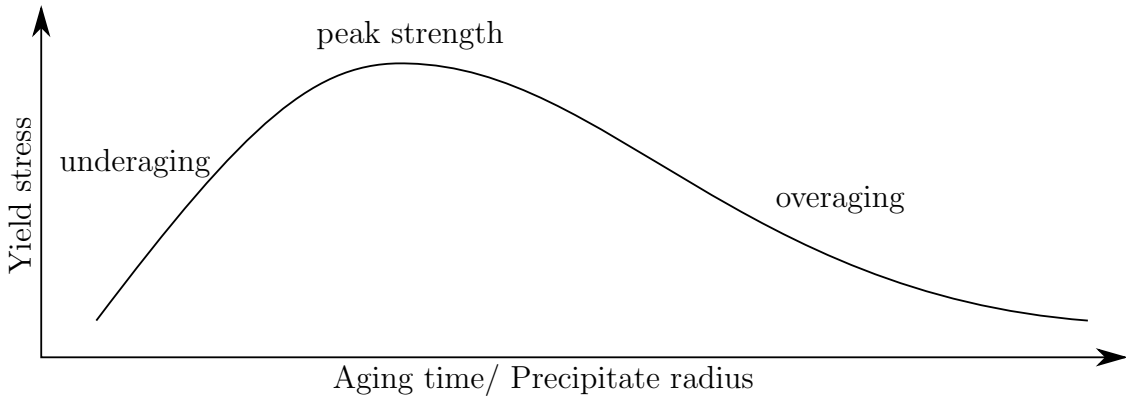

Figure 4: Yield stress versus aging time schematically. Initially the yield stress increases since shearing of the precipitates becomes increasingly difficult when they grow. Further aging, after precipitates become incoherent cause the yield stress to drop.

second phase particles (copper for 17-4PH) begins – underaging. Figure 4 shows a typical hardening curve, the yield stress depending on the precipitates radius, which is a function of the aging time. The yield stress is that stress when dislocations start to travel long distances and plastic deformation can be observed. During the second stage the precipitates grow until an equilibrium precipitate volume fraction is reached – peak strength. A bigger precipitates radius increases the impediment of dislocation motion as described later. In the third stage a coarsening of precipitates, with large particles growing at the expense of small ones occurs – overaging – which leads the yield stress to drop. Additionally, after reaching a specific size the precipitates become incoherent within the matrix, the material softens.

As mentioned the hardness of a material depends on the interaction of precipitates and dislocations. Dislocations are line defects where atoms are out of position in the crystal structure. The Burgers vector $\vec{b}$ quantifies the misalignment, and gives the vector which is necessary to close a atom-by-atom loop around the dislocation, if this path is made in a perfect crystal the loop isn't closed and the Burgers vector is necessary to close the path. When the stress on a metal is high enough, dislocations start to move which results in a plastic deformation of a body. But, the motion of

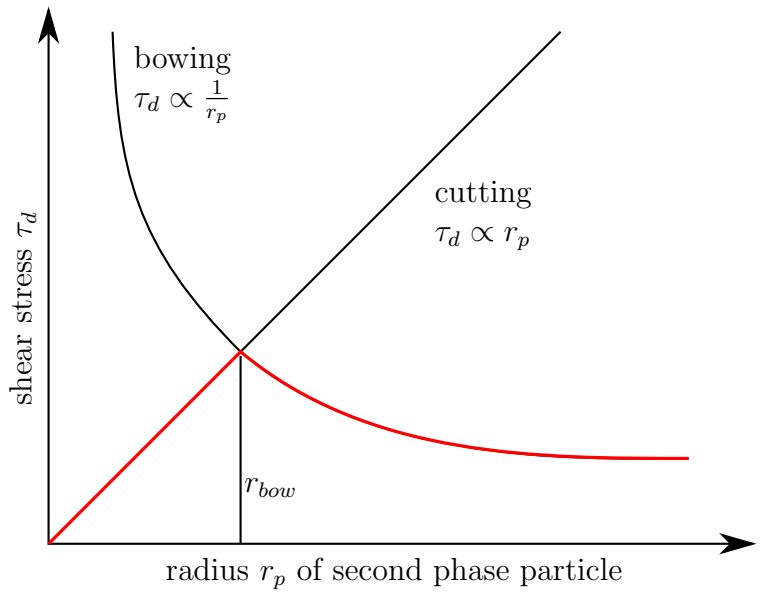

Figure 5: Strengthening of a material, due to dislocation obstacles interaction depending on the particle radius.

dislocations is influenced by the presence of obstacles like precipitates. The critical stress necessary to overcome an obstacles depends for example on their size, density, coherency, crystal structure and chemical characteristic.

There are different ways of interaction between dislocations and obstacles. For a small obstacle size the dislocation gets cut. With increasing precipitate radius r_p a higher shear stress is necessary to overcome this obstacle. For $r_p > r_{bow}$ bowing of the dislocations is dominant. Figure 5 shows the shear stress necessary for a dislocation to overcome an obstacle depending on its particle size.

In general, the gliding dislocation bows out between precipitates as shown in Figure 6. The force balance between the pinned dislocation and the obstacles is given by

$$F_p = 2T \cos\left(\frac{\phi_c}{2}\right), \tag{21}$$

where F_p is the maximum resisting force of a precipitate, T is the line tension of the dislocation, and ϕ_c the critical angle just before a dislocation breaks away.

The applied shear stress τ_d forces the dislocation into an arc of radius R as

$$\tau_d \vec{b} = \frac{T}{R} \,. \tag{22}$$

The radius of the curvature and the distance between the precipitates is linked by

$$2R\sin(\theta) = L_p \,, \tag{23}$$

in addition $\theta = 90° - \phi/2$ which can be simplified because of the symmetry of the trigonometric functions to

$$\tau_d \vec{b} = \frac{2T\cos\left(\frac{\phi}{2}\right)}{L_p} \,. \tag{24}$$

Substituting equation (21) into (24) yields for the critical shear stress τ_c

$$\tau_c = \frac{2T\cos\left(\frac{\phi_c}{2}\right)}{\vec{b}L_p} \,. \tag{25}$$

If we assume a constant distance between precipitates, equation (25) predicts for larger precipitates a higher increase in the hardening effect than for small precipitates. As seen before in Figure 4, if the size per precipitates is getting to large the distance between the obstacles decreases and therefore a short aging time and therefore smaller precipitates can strength the material more.

Figure 7 shows the Orowan mechanism which occurs for very large precipitates. First, the dislocation gets bowed between the precipitates then by-passing the obstacles a dislocation loop forms around each precipitate.

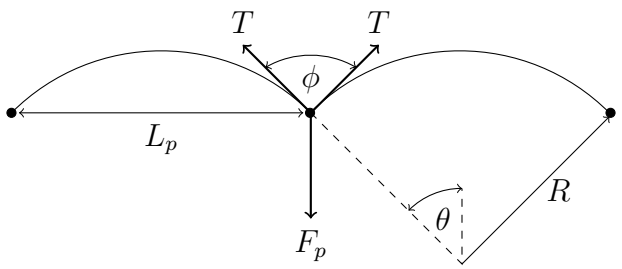

Figure 6: Force balance between the pinned dislocation and obstacles [18].

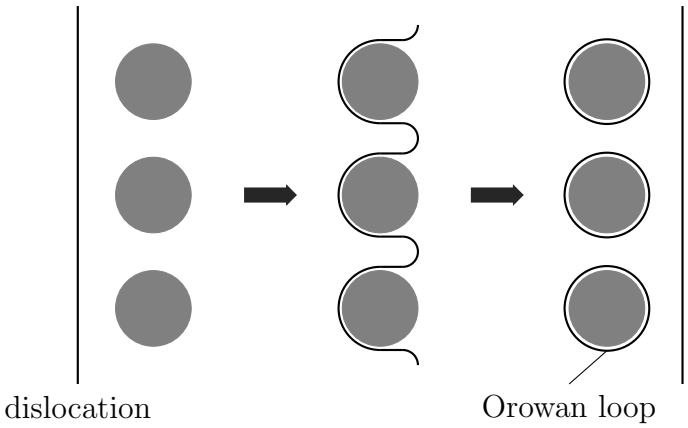

Figure 7: Orowan mechanism, the dislocation line continues to bend around the particle until it is enclosed completely and the dislocation can move on, leaving a dislocation ring around the bypassed particle (simplified from [17]).

2.4 Hysteretic Dislocation Movement

Granato and Lücke [6] proposed a model which predicts the nonlinear hysteretic response of metals. It describes the interaction of a dislocation line segment pinned to obstacles. If an external stress is applied, there is an elastic strain and in addition a dislocation strain. The stress-dislocation strain is a function of the frequency, but constant for low frequencies in the kilohertz range. The interaction of a dislocation line with obstacles for an increasing applied stress is shown in Figure 8(a). For a no stress the dislocation line is pinned by the impurity particles (A), with increasing stress they bow out (B). In this range the stress dislocation strain is proportional to the obstacles distance L_p. When the shear stress overcomes the critical stress the dislocation breaks away (C-D), which yields to a rapid increase in the strain without increasing the stress. As the stress increases the dislocation bows out along the length L_N (D-E), the effective modulus is given by this length. Finally the dislocations starts to get disconnected from all impurities in a closed dislocation loop (F-G). The formation of this dislocation loops is an irreversible process. The corresponding qualitative stress strain curve is shown in Figure 8(b). A hysteretic loss can be observed during decreasing stress (D-A), there the long loop collapses

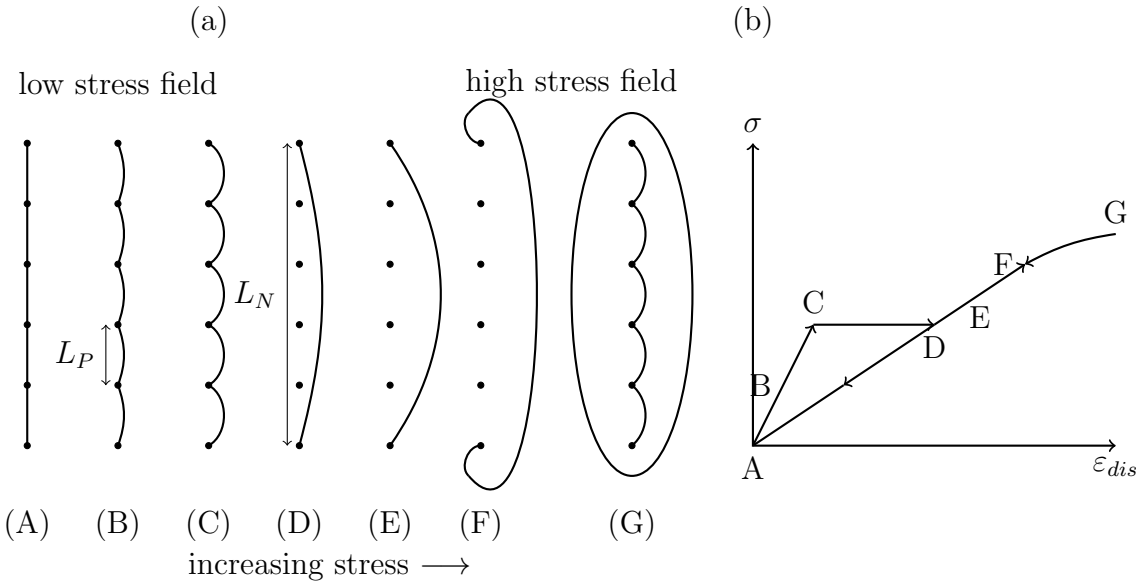

Figure 8: (a) Schematically the procedure of bowing out of a pinned dislocation under an increasing stress, and their breakaway. (b) Solid line shows the dislocation strain in each step from (a). The path A-F shows the behavior for increasing and F-A for decreasing stress [6].

elastically along a path determined by the long loop length, which closes the stress-strain relation and shows a similar hysteretic behavior as explained for the PM space.

2.5 Equation of Motion for a Resonant Bar

This section derives the resonance frequency shift in a resonant bar due to hysteretic elements as shown by Guyer et. al [7].

For a pure longitudinal compression mode, with an external force $f(x,t)$, the equation of motion is given as

$$\frac{\partial^2 u}{\partial t^2} + \frac{1}{\tau}\frac{\partial u}{\partial t} = \frac{1}{\rho}\frac{\partial \sigma}{\partial x} + \frac{f(x,t)}{\rho}\,, \tag{26}$$

where the second term on the left is a simple damping term proportional to the relaxation time τ.

As we have seen in equation (18) the stress in a material with a hysteretic behavior, is the sum of the stress due to classical nonlinearity from lattice anharmonicity

$$\sigma_A = K_0\left[\varepsilon + \beta\varepsilon^2 + \delta\varepsilon^3 + \dots\right]\,, \tag{27}$$

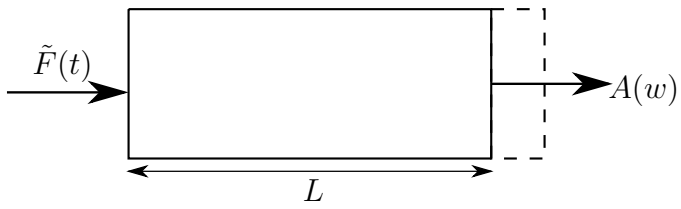

Figure 9: Sketch of a resonant bar.

and hysteretic elastic elements contribution [23]

$$\sigma_H = K_0\alpha\left[-\varepsilon_m\varepsilon + \frac{\mathrm{sgn}(\dot{\varepsilon})}{2}\left(\varepsilon_m^2 - \varepsilon^2\right) + \dots\right], \tag{28}$$

where K_0 is the linear modulus, β and δ are the quadratic and cubic classical nonlinearity parameters [16] and ε is the strain field. ε_m is the maximum strain, the signum of the strain rate is given by $\mathrm{sgn}(\dot{\varepsilon})$ and α gives the strength of the material hysteresis. Therefore, the stress field in a bar under the assumption that hysteretic nonlinearity is dominant, is given by

$$\begin{aligned}\sigma &= \sigma_A + \sigma_H \\ &= K_0\left[\varepsilon - \alpha\varepsilon_m\varepsilon + \mathrm{sgn}(\dot{\varepsilon})\frac{\alpha}{2}\left(\varepsilon_m^2 - \varepsilon^2\right) + \dots\right].\end{aligned} \tag{29}$$

The classical nonlinearity terms are omitted because they are much smaller than the effect of hysteresis in nonlinear term. For a resonant bar (length L), as shown in Figure 9, which is exited on one end with a force f , and the movement is measured on the opposite side, the equation of motion for the displacement field u is given by

$$\rho\frac{\partial^2 u}{\partial t^2} + \frac{\rho}{\tau}\frac{\partial u}{\partial t} = \frac{\partial \sigma}{\partial x} + f(t)\frac{L}{2}\Big[\delta\Big(x + \frac{L}{2}\Big) - \delta\Big(x - \frac{L}{2}\Big)\Big], \tag{30}$$

where $\delta(x)$ is the delta function and not the cubic nonlinearity parameter in equation (27). Instead of using the displacement u, the equation of motion at the bar center can be rewritten in terms of the strain ε using a lumped element model [9]:

$$\ddot{\varepsilon} + \frac{1}{\tau}\dot{\varepsilon} = -\frac{\pi^2\sigma}{4L\rho} - \tilde{F}(t) \tag{31}$$

The equation of motion can be rewritten by combining equation (29) and (31) and has a similar form to a damped oscillator

$$\ddot{\varepsilon} + \frac{1}{\tau}\dot{\varepsilon} = -\omega_0^2\left(\varepsilon - \alpha\varepsilon_m\varepsilon + \mathrm{sgn}(\dot{\varepsilon})\frac{\alpha}{2}(\varepsilon_m^2 - \varepsilon^2)\right) - \tilde{F}(t)\,, \tag{32}$$

where ω_0 is the linear resonant frequency of the bar, and ε_m gives the maximum strain in the bar. The response of interest is the the strain at the opposite end of the bar at the driving frequency of the force ω and its dependency of the amplitude F_0. For solving the equation of motion, we assume the force $F(t)$ has the form

$$\tilde{F}(t) = F_0 \sin(\omega t + \phi)\,. \tag{33}$$

This leads to a strain in the bar

$$\varepsilon(t) = R\sin(\omega t), \qquad \varepsilon_m = R\,. \tag{34}$$

By substituting equation (33) and (34) into (32), and project it onto a space with the bases $\sin(\omega t)$ and $\cos(\omega t)$, the sin term equals

$$-\omega^2 R = -\omega_0^2(1-\alpha R) - F_0\cos(\phi) - \omega^2 R^2 \frac{\alpha}{2}\Big\langle \sin(\omega t)|\mathrm{sgn}\big(\cos(\omega t)\big)\cos^2(\omega t)\Big\rangle\,. \tag{35}$$

And the cos-projection is

$$\frac{\omega}{\tau}R = -F_0\sin(\phi) - \omega_0^2 R^2\frac{\alpha}{2}\Big\langle \cos(\omega t)|\mathrm{sgn}\big(\sin(\omega t)\big)\cos^2(\omega t)\Big\rangle\,. \tag{36}$$

The projection $\langle a|b\rangle$ is defined as

$$\langle a|b\rangle = \frac{1}{T}\int_0^T \mathrm{d}t\, a(t)\, b(t)\,, \tag{37}$$

where $T = 2\pi/\omega$. The numerical values for the projections in equation (35) and (36) are

$$\Big\langle \sin(\omega t)|\mathrm{sgn}\big(\cos(\omega t)\big)\cos^2(\omega t)\Big\rangle = 0\,, \tag{38}$$

and

$$\Big\langle \cos(\omega t)|\mathrm{sgn}\big(\sin(\omega t)\big)\cos^2(\omega t)\Big\rangle = \frac{4}{3\pi}\,. \tag{39}$$

Thus equation (35) and (36) can be simplified as

$$-\omega^2 R + \omega_0^2(1-\alpha R)R = -F_0\cos(\phi)\,, \tag{40}$$

and

$$\frac{\omega}{\tau}R + \omega_0^2 \frac{2}{3\pi}\alpha R^2 = -F_0 \sin(\phi)\,. \tag{41}$$

In equation (40) and (41), R and ϕ are unknown and have to be solved for, therefore $\Omega = \omega_/\omega_0$ is used, which gives the normalized frequency relative to the linear resonance frequency. Thus it follows

$$R = \frac{F_0}{\sqrt{(\Omega^2 - (1-\alpha R)^2)^2 + \left(\frac{\Omega}{\Omega_0} + \frac{4}{3\pi}\alpha R\right)^2}}\,, \tag{42}$$

where $Q_0 = \omega_0 \tau$ equals the damping factor at the resonance frequency.

Thus the equation of motion can be solved for the normalized frequency shift, which is proportional to α

$$\delta\Omega = -\frac{\alpha R}{2}\,. \tag{43}$$

Additionally, an increase in the attenuation factor proportional to α is observed

$$\delta\frac{1}{Q} = -\frac{1}{Q} - \frac{1}{Q_0} = \frac{4}{3\pi}\alpha R, \qquad \Omega \approx 1\,. \tag{44}$$

Since R is the amplitude of the periodic strain ε, it equals half the peak to peak amplitude $\Delta\varepsilon$. When the stress sweeps over σ, the strain can be split up in a linear strain $\varepsilon^{(1)}$ and a nonlinear part $\varepsilon^{(3)}$ which is proportional to the number of hysteretic elastic elements involved

$$\Delta\varepsilon \approx \varepsilon^{(1)} + \varepsilon^{(2)} \approx \frac{\sigma}{K}\,. \tag{45}$$

This means for a increasing stress, more and more hysteretic elastic elements are involved. If more hysteretic elastic elements are involved the strain is increasing and therefore a higher frequency shift can be observed.

Other researchers [10] [30] normalized the frequency shift by f_0, which is the resonance frequency for a infinitesimal small amplitude, and express the frequency shift in terms of $\Delta\varepsilon$

$$\frac{\Delta f}{f_0} = \frac{f - f_0}{f_0} = \alpha\Delta\varepsilon\,, \tag{46}$$

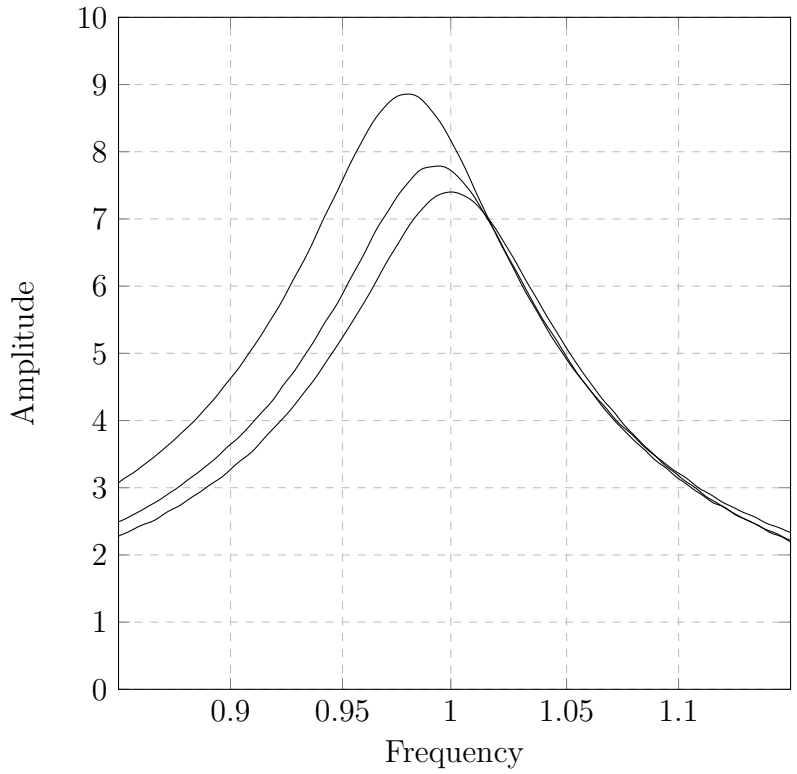

Figure 10: Resonant response of bar with hysteretic elements.

the same expression to present α is used for the measurements done in this research.

Figure 10 gives a theoretical prediction how the resonance response of a hysteretic bar changes with increasing driving amplitude. The y-axis in Figure shows the response and the x-axis the normalized frequency. As we can see for a increasing driving force the resonance frequency is shifted towards a lower frequency furthermore, the damping increases.

In [31] it is shown that the nonlinearity parameter α differs depending on the analyzed mode shape. The material softening in longitudinal modes (α_E) is much higher than for torsional modes (α_G) which is shown both theoretically and in an experiment. This underlines the tensorial nature of the fast dynamics response for hysteretic elastic materials.

CHAPTER III

NONLINEAR ULTRASONIC RESONANCE SPECTROSCOPY FOR SMALL SAMPLES

3.1 NRUS Experimental Setup

The nonlinear resonance ultrasonic spectroscopy measurement setup as shown in Figure 11, tracks the resonance behavior of small rectangular plates (10mm x 10mm x 2mm). A piezoelectric transducer excites a longitudinal wave sweeping through a user specified frequency range. For the purposes of NRUS, the sample is usually excited at a constant amplitude swept sine fashion.

The specimen which is in line contact along one edge with the transducer starts to vibrate at it's resonance frequency. The holder fixes the specimen such that the contact condition between specimen and holder is minimized along two lines at the edge of the fixture, and the specimen is clamped to the transducer by four screws. The out of plane velocity of the specimen is captured by a laser vibrometer. The signal is recorded on an oscilloscope, sampled at around 100kSa/s. The data is transferred to a computer, where post-processing of the recorded data can be conducted for further analysis. After finishing a specified number of sweeps, the amplitude of the sinusoidal signal is changed, and the measurement is repeated.

The whole setting is controlled by LabVIEW program which specifies the excitation parameters, stores the measured data and repeats this process for different amplitudes. Finally, the data is post-processed in Matlab as described in section 3.2.

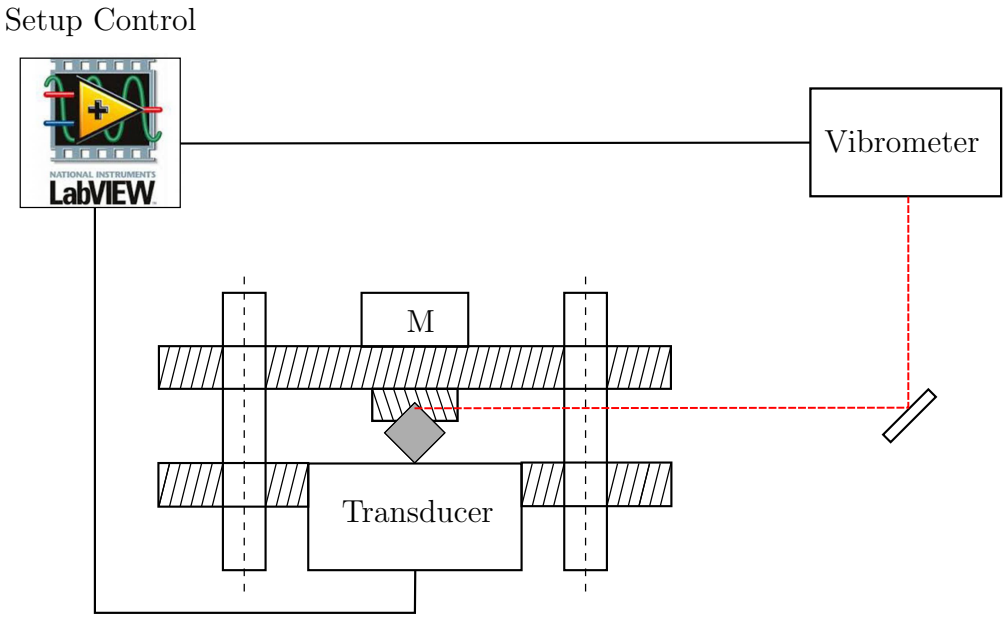

Figure 11: Sketch of a used experimental setup.

3.1.1 Function Generator

A function generator Agilent 33250A is used to obtain a sinusoidal signal. The sinusoidal signal is swept in a given sweeptime through a user specified frequency range that corresponds to the expected resonance of the sample. During the sweep the function generator increases the frequency constantly until it reaches the higher bound of the frequency range. For the NRUS experiments the excitation frequency is varied between a peak to peak voltage of 1 and 20V. An internal trigger is used to distinguish different sweeps in the post processing, therefore the trigger signal is connected to the oscilloscope.

3.1.2 Transducer

The emitting transducer needs to be able to drive the sample at high amplitudes, therefore a high power, high frequency type of transducer is used. For this experiments a Ultran GRD50-D50 piezoelectric transducer with a nominal frequency of 50 kHz is used to excite the sample. The transducer converts the incoming electrical signal of the function generator into a longitudinal wave.

3.1.3 Laser Vibrometer

A laser vibrometer allows one to make non-contact measurements of the velocity of a moving surface. The laser vibrometer is the key piece of equipment in the experimental design of NRUS. In general, the laser vibrometers allow for the sample measurements to be taken without mass-loading the sample and can detect relatively small velocities, $\approx 0.1\,\mu m/s$. These devices are used in a variety of applications, from insect communication to nondestructive evaluation. The general principle behind the laser vibrometer is interferometry, in which waves are superimposed into order to determine information about the waves. The Doppler shift is the primary physical principle utilized in laser vibrometer measurements and is illustrated in Figure 12.

The Doppler shift is given by the following formula [32]:

$$\delta v = \frac{2|\vec{u}|}{\lambda}\cos(\gamma)\sin((\pi-\zeta)/2) = \frac{2|\vec{u}|}{\lambda}\cos(\gamma)\cos(\zeta/2) \tag{47}$$

where γ is the angle between the velocity vector of the surface and the its normal component. ζ is the angle between the incident and reflected beam. However in practice, ζ is usually nearly zero (at most, 1-2°) , so the last term goes to one, leaving:

$$\delta v = \frac{2|\vec{u}|}{\cos(\gamma)} \tag{48}$$

A general schematic of a laser vibrometer is shown in Figure 13 below. The

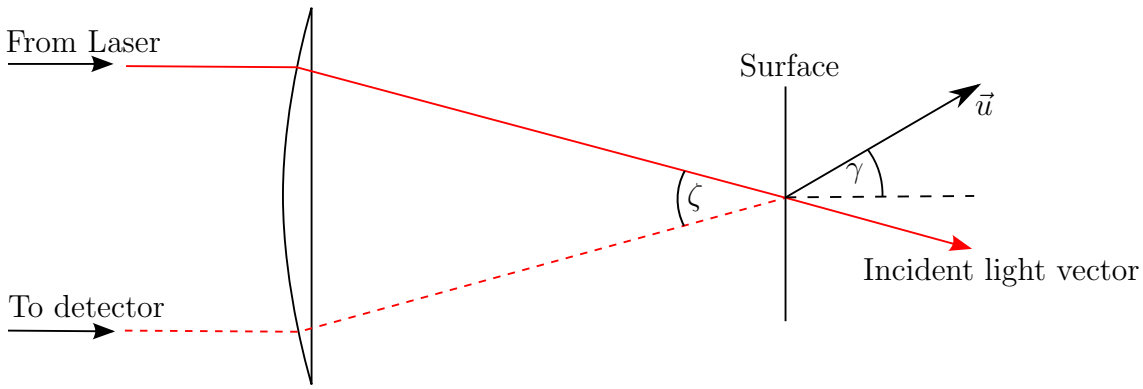

Figure 12: Schematic of the Doppler shift phenomenon (adapted from [32])

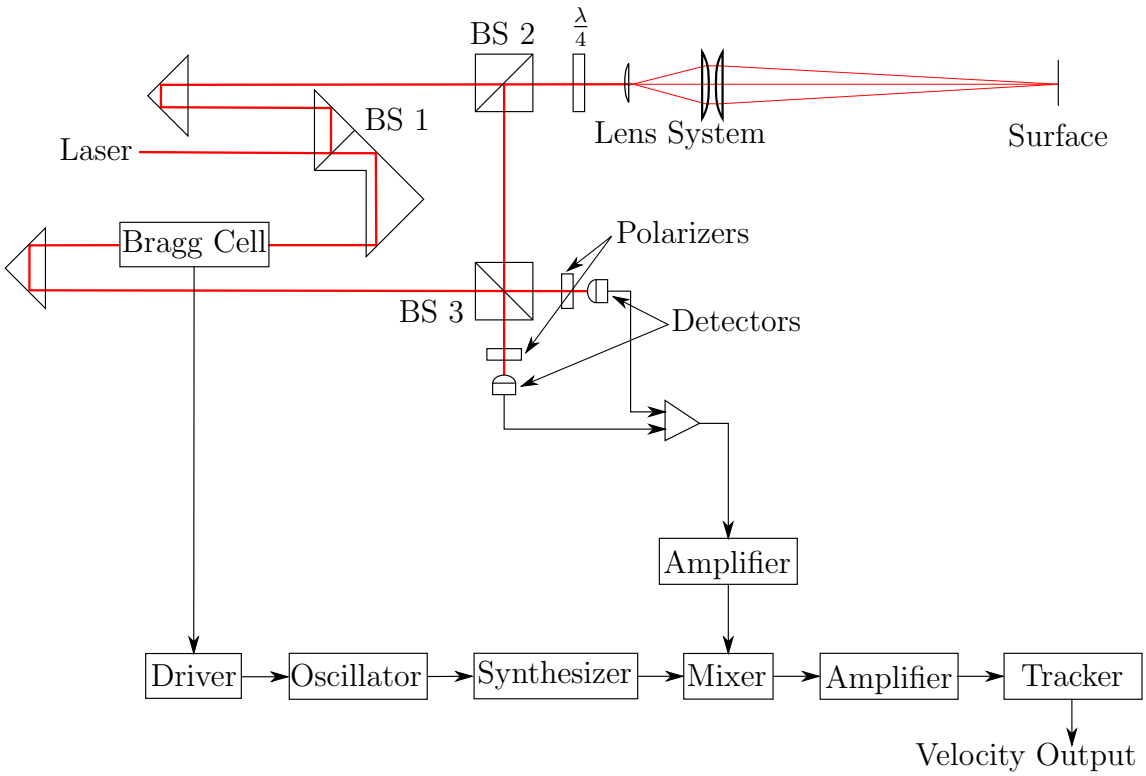

Figure 13: Laser vibrometer schematic (adapted from [32]).

frequency of the laser is first split by a beam splitter (BS 1) into a reference beam, which goes directly to the photo detector, and a test beam which is sent towards the target. Because the target has some out of plane velocity, u, the reflected light beam has now been Doppler shifted. Both the reference and reflected beams are shifted by an acousto-optic modulator, commonly called a Bragg cell, which shifts the beams via sound waves, usually radio waves ($\approx 30 - 40$ MHz). The signal is picked up by the detectors, which go through a series of post-processing steps before outputting the velocity measurement.

The Bragg cell is necessary for several reasons. With simple interferometry (with no phase shift), there will be sign ambiguities in the relation of frequency to the velocity of the surface. By shifting the frequency by more than the maximum value of the Doppler shift, the frequency at the detector is never zero, which avoids the issue of sign ambiguity. In practice, the Doppler shift is around 10 MHz or higher,

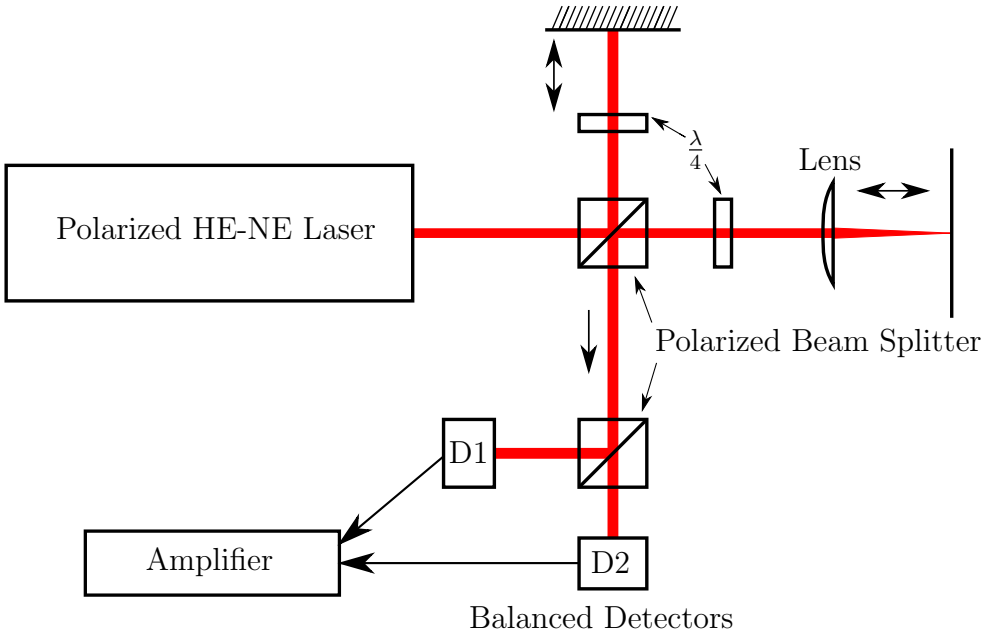

Figure 14: Balanced detector design (adapted from [32])

while the typical Bragg cell has a frequency shift of 40 MHz.

The detectors are arranged in a balanced design, which is shown in Figure 14 below. Balanced here refers to the signals, which are balanced in the sense that the two signals are directly referenced to each other rather than to ground or pseudo-ground. Quarter wave plates are polarizers which ensure the signal is orthogonal to the beam splitter.

The signal is pre-amplified near the sensor to reduce noise in the signal. Then the signal is mixed down since it can not be processed at such a high frequency. The signal is pre-amplified again before being sent to a frequency tracker to further reduce noise in the signal.

Further the Polytech Laser Vibrometer (OFV-5000) provides integrated low- and high-pass filters, for the analayzed frequency range a high-pass filter of 100 Hz and a low-pass filter at 100kHz are used.

3.1.4 Data Acquisition

The electrical output signal of the Polytech Laser Vibrometer as well as the trigger signal are recorded by a Tektronix 5034B oscilloscope, sampled at 100 kSa/s. Each sweep is repeated at least 9 times to reduce the error in the peak detection during the post-processing as explained in section 3.2.

3.2 Measurement Protocol and Signal Processing

In the following, the complete measurement protocol is explained based on an example including all experimental and signal processing steps. The experimental parameters used are developed in preliminary experiments and are discussed in detail in section 3.3. This example is used to familiarize the reader with the technique and steps used in this research.

First, a small rectangular plate (10mm x 10mm x 2mm) specimen is exited over a large frequency band (between 30 and 45 kHz) in order to detect the resonance modes of the sample geometry in the setup system. Each peak represents a resonance frequency of the rectangular specimen. For the further analysis, the resonance mode with the lowest damping – the narrowest resonance response – is chosen. This frequency, which is usually between 35 and 36.5 kHz, is used for all specimens with the given plate geometry. The purpose of fixing this resonance mode helps compare the results of different heat treated samples with similar plate geometry. As shown in equation (46), the nonlinearity parameter α is defined over the strain ε, but due to the high frequencies used and the missing information about the elastic properties of the specimens, it is not possible to determine or simulate the strain in the specimens. To overcome this drawback, the frequency range, and therefore the resonance mode, is kept constant; it can be assumed that the strain at the same measurement position has the same proportionality between strain and velocity. So, the results of the measurements performed are not the absolute nonlinearity parameter α as defined

in the literature, which can be determined only if the strain is accurately measured. Further, as shown in Section 2, α is different for longitudinal and torsional modes. In Section 3.6 the mode shape for the used configuration is shown; it is a combination of a longitudinal and torsional vibration therefore, the strain is a linear combination

$$\Delta\varepsilon = a_E \Delta\varepsilon_E + a_G \Delta\varepsilon_G \,, \tag{49}$$

where ε_E represents the longitudinal strain and ε_G the torsional strain and a_E and a_G give their fraction of the absolute strain. The same linear combination is given for the velocity

$$\Delta v = b_E \Delta v_E + b_G \Delta v_G \,, \tag{50}$$

where b_E and b_G are constants which give the fraction of longitudinal and torsional velocity. So for this research a α' is measured which is a combination of α_E and α_G, and a function of the measured velocity. This approach will meet the objective of this research which is to check if NRUS is capable of detecting changes in the microstructure. For notational simplicity in the rest of this work instead of α', the term α will be used. As all experimental parameters are set constant for all specimens, it is reasonable to assume that changes in the frequency shift are only due to the material nonlinearity. This allows us to compare differences in the nonlinearity parameter α, and then link them to changes in the material microstructure.

Each specimen is fixed with a pressure which is similar to a force of 20 Newtons. For this example, vacuum grease is used as a couplant. The excitation transducer provides a frequency sweep between 35 and 36.5 kHz in a sweeptime of 2 s. For each driving amplitude, this frequency sweep is performed 9 times. After these 9 sweeps, the driving amplitude, of the frequency generator is increased by 1V. A full measurement set consists of 20 measurements at a output voltage of the frequency generator between 1 and 20 V. Figure 15 shows a typical time domain signal of the specimen response for one sweep. As the 9 sweeps are measured in a row, the trigger

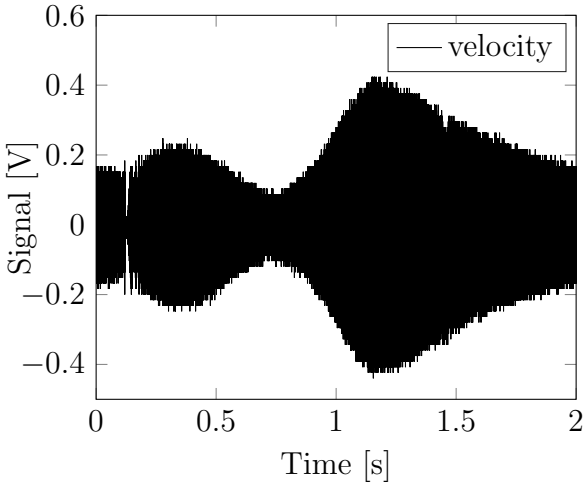

Figure 15: Time domain signal

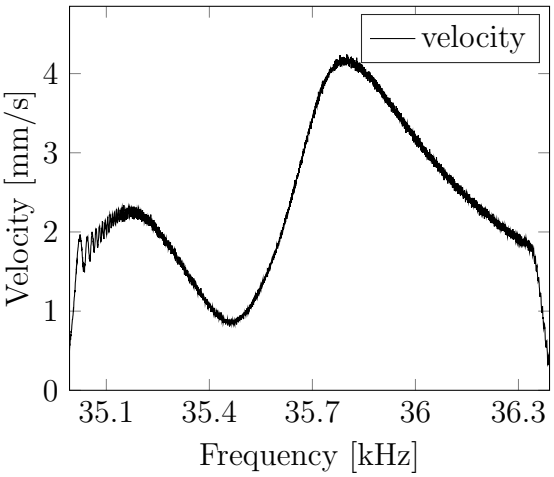

Figure 16: FFT of the velocity

signal is used to cut them into single sweeps. Each single sweep time domain signal is Fourier transformed into the frequency domain (see Figure 16), where the x-axis shows the excited frequencies and the corresponding velocity response on the y-axis.

Since this result is still very noisy, the signal gets filtered by applying a moving average filter as shwon in Figure 17. The crucial information which should be extracted from this frequency response is the resonance frequency and its corresponding velocity. To do so, a 5th oder polynomial is fitted around the maximum of the filtered response curve and its maximal turning point is used to store the resonance frequency and its velocity as shown in Figure 18.

Figure 19 shows a typical NRUS result, where each line represents the average frequency response of 9 sweeps at a certain driving amplitude and the average resonance frequency peak is marked by a asterisk. Obviously for an increasing driving amplitude, the velocity response increases, but the resonance frequency also gets shifted to a lower frequency. This resonance frequency shift is due to the nonlinearity of the material. The black line shows a linear fit through the peaks and is needed to determine the used start frequency f_0 in equation (46), where f_0 equals the intersection of the linear fit and the x-axis and gives the resonance frequency for an infinitesimal

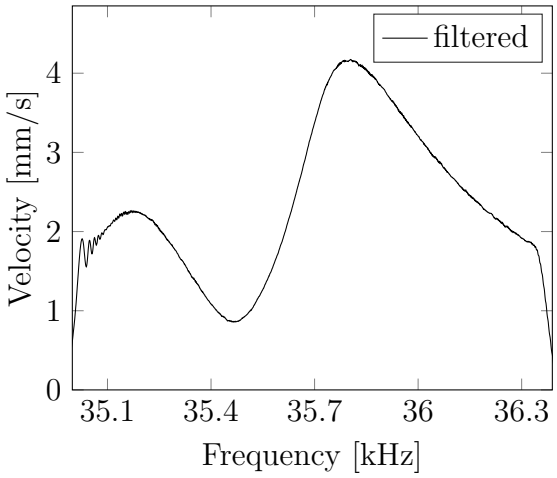

Figure 17: Filtered FFT

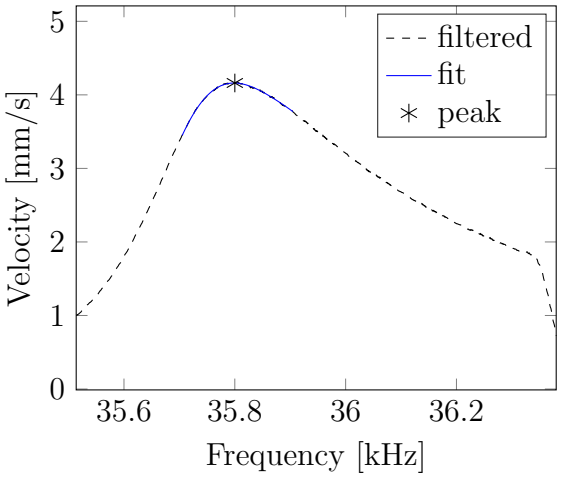

Figure 18: Peak fit and find maximum

small excitation.

To simplify the visualization of the nonlinearity parameter, α another common graphic is introduced here and used in the rest of this thesis to present experimental results. To do this, the frequency shift $\Delta f = f - f_0$ for each excitation is divided by f_0, displayed on the y-axis, and the peak velocity is used as the corresponding x-coordinate. Therefore, the nonlinearity parameter α is directly proportional to the slope of a linear fit in this presentation, as shown in Figure 20. The errorbars represent the standard deviation from the mean of these 9 sweeps regarding the resonance frequency detection. Finally, a linear fit is performed and its slope gives the nonlinearity parameter α. On top of the graph you can see the corresponding function of the fit and its coefficient of determination R^2.

3.3 Preliminary Studies for System Nonlinearity

Before NRUS is used for characterizing thermal damage in 17-4PH stainless steel different experiments are done to validate the accuracy of the developed setup.

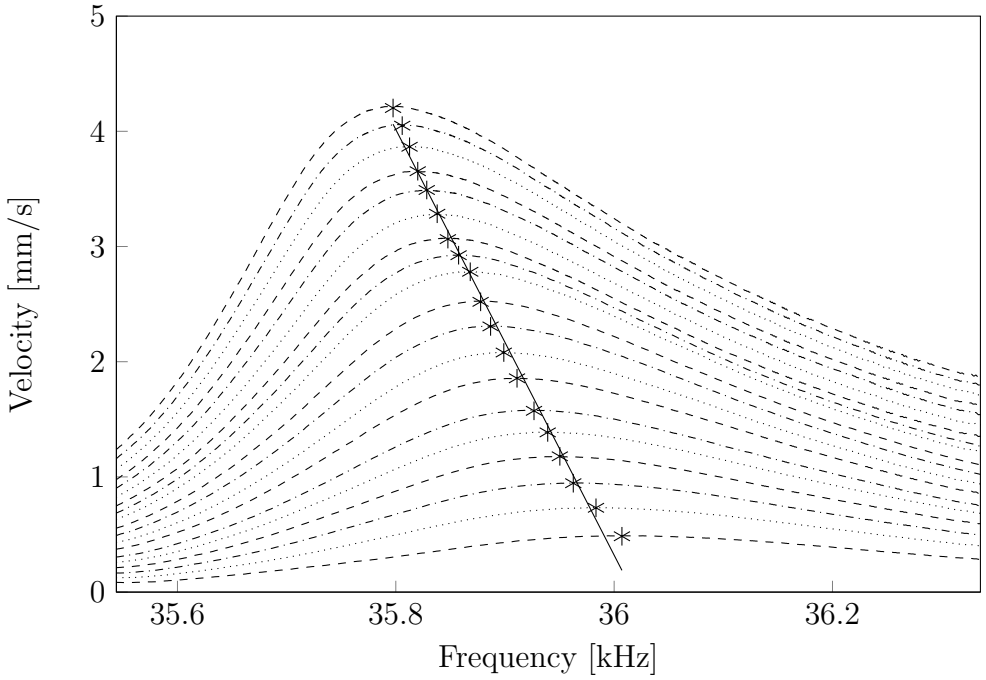

Figure 19: Example response for different driving amplitudes.

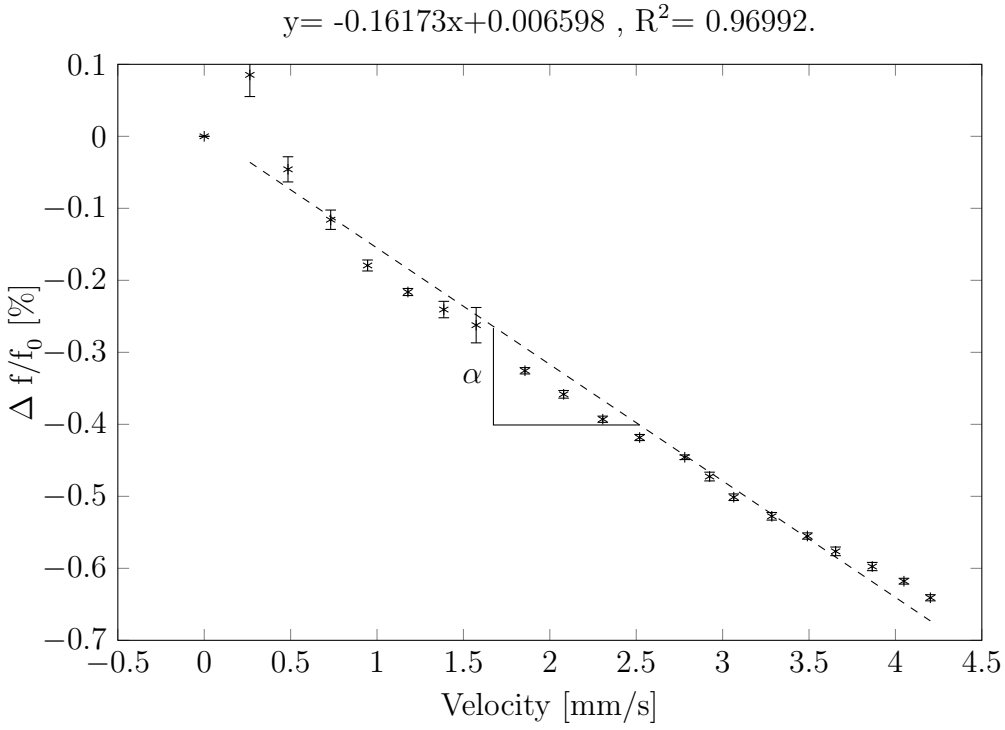

Figure 20: Relative frequency shift for the in Figure 19 shown frequency responses.

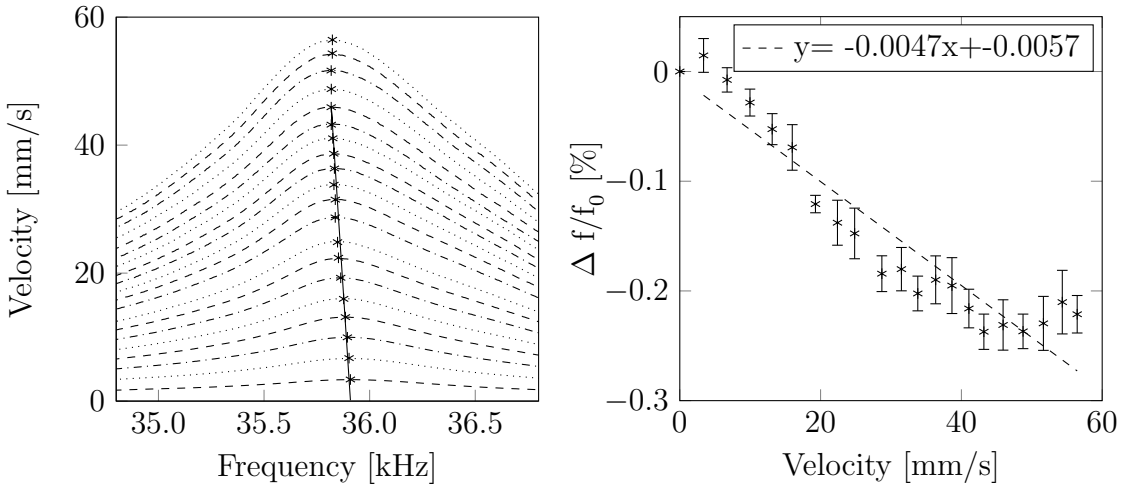

Figure 21: Frequency response and nonlinearity parameter α of the transducer

3.3.1 Transducer Nonlinearity

For the determination of the nonlinearity parameter α the nonlinearity of the transducer in the frequency band of interest has to be known. In Figure 21 the frequency response and the frequency shift for a higher excitation is illustrated. As we can see in Chapter 5 the measured nonlinearity of the transducer $\alpha = -0.0047$ is at least one order smaller than the nonlinearity of the measured samples. A deeper discussion about system nonlinearity of the used setup is given in Section 3.5.

3.3.2 Force

A important condition is the pressure between the specimen and the transducer. It influences the contact condition between the specimen and the fixture as well as the transducer. In a previous experiment for a plexiglas fixture is was seen that the line contact transforms into area contact after a couple of experiments if the pressure is too high. This flat edge increases the damping of the fixture and lower velocities were measured. This change of the experimental setup should be avoided, because it influences the measured nonlinearity due to changes in the contact condition. A detailed discussion about material influences of the holder is given in the next section.

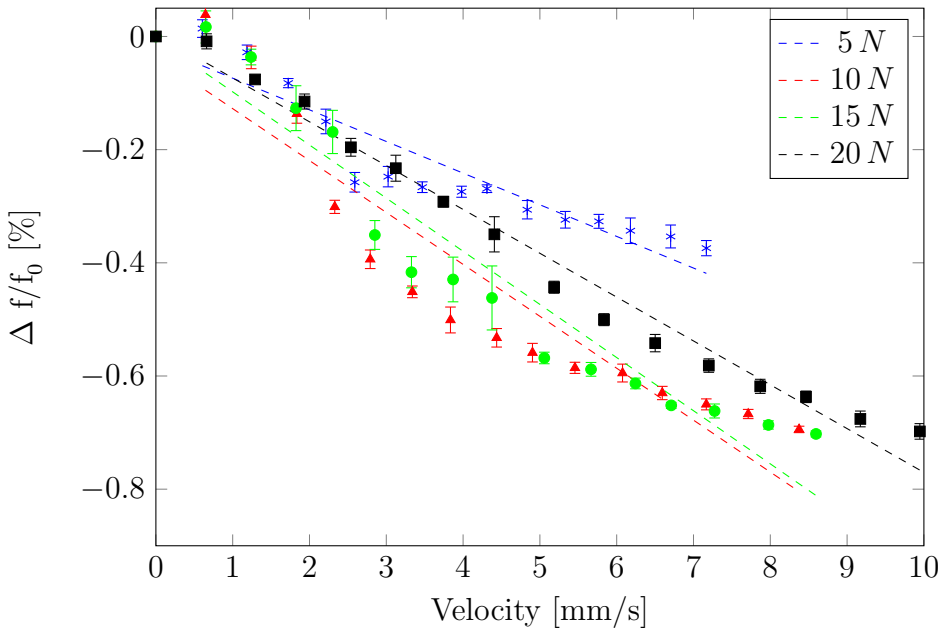

Figure 22: Dependency of the frequency shift for different weights forcing the specimen on the transducer.

Table 1: Nonlinearity Parameter for different forces

Force	α	R^2
5 N	-0.05592	85.4 %
10 N	-0.09175	86.0 %
15 N	-0.09391	91.7 %
20 N	-0.07745	97.8 %

For the results in Figure 22 the experimental setup shown in Figure 11 is used and the acting gravitational force is varied. In general huge differences in the nonlinearity parameter α but no directed trend can be observed. In Table 1, α for each measurement and the coefficient of determination R^2, which is a measure of the quality of the fit is given.

For R^2 a linear increase for higher pressure can be seen, this means the linear fit of the frequency shift fits better to the measured data. As seen in Chapter 2 the theoretical model predicts this linear frequency shift, consequently for higher forces the results match better with the theoretical prediction. This can be explained by some changing contact conditions especially for higher excitations where the contact may

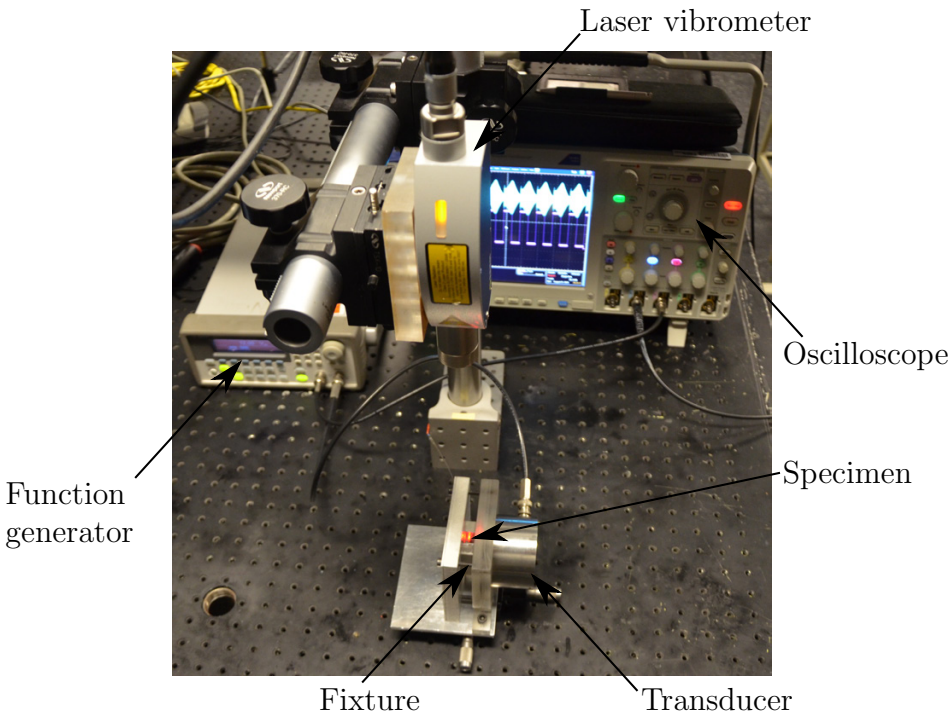

Figure 23: Used experimental setup.

be disturbed as we can see in Figure 22 for higher velocities the relative error from the fit is higher. In addition, for excitation the reached maximum velocity increases which supports the assumption of a better contact condition between the transducer and the specimen.

In conclusion, the acting pressure between transducer and specimen is a crucial parameter and has to be controlled in the experiment, because it directly changes the measured α. Therefore, a pressure sensor is integrated in the experimental setup which measures the pressure acting on the specimen. Due to a simplification of the experimental setup the fixture is pushed against the transducer by four 10x32 screws, as shown in Figure 23. The pressure sensor measures the force in the center of the fixture which is equal to the one acting on the specimen. Further, the setup is rotated by 90° so that the laser vibrometer is placed vertical above the sample and no mirror is necessary.

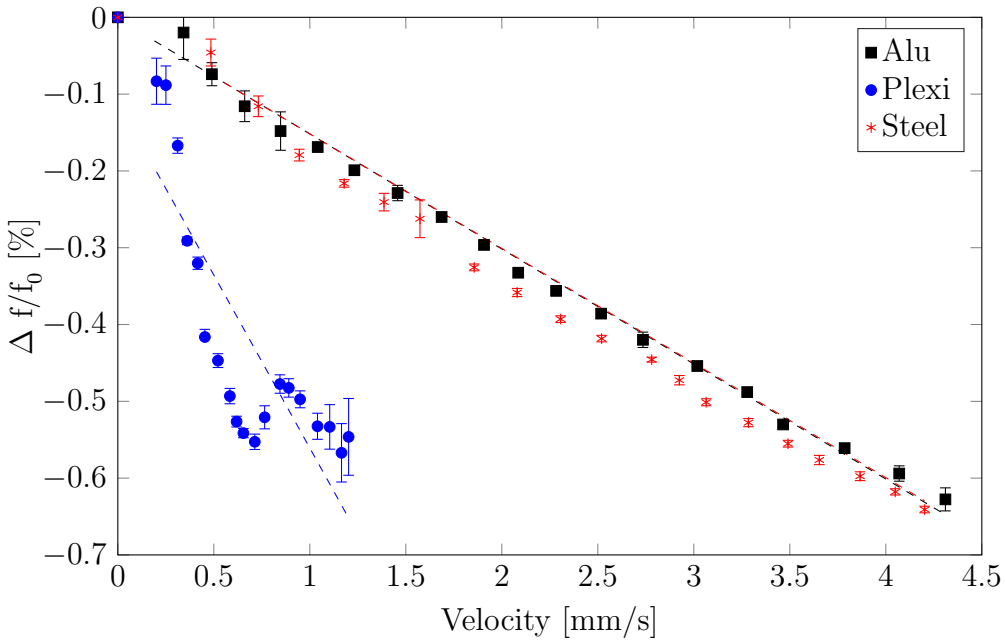

Figure 24: Comparison of different fixture materials and their effect on the measured nonlinearity. Aluminum and stainless steel show the same the result whereas Plexiglas changes the measured nonlinearity.

3.3.3 Fixture Material

The sample fixture is a crucial part, because it is the only part which is in contact with the specimen. It is designed to reduce the contact area as far as possible, which should reduce the impact of contact nonlinearity in the experiment. Due to the small sample geometry it is even more important to reduce non-material nonlinearity effects than it is in other experiments.

To determine the effect of the fixture material a aluminum, a stainless steel and a plexiglas fixture with the same design were manufactured. As shown in Figure 24 the fixture material has an impact on the slope and hence on α. The slope for the plexiglas fixture is steeper than for the other two materials, this means a similar frequency shift is reached at a lower velocity. In general the velocity response is smaller, maximal 1.2 mm/s compared to 4.5 mm/s for aluminum and stainless steel, which concludes that for plexiglas the specimen is highly damped. This assumption can be

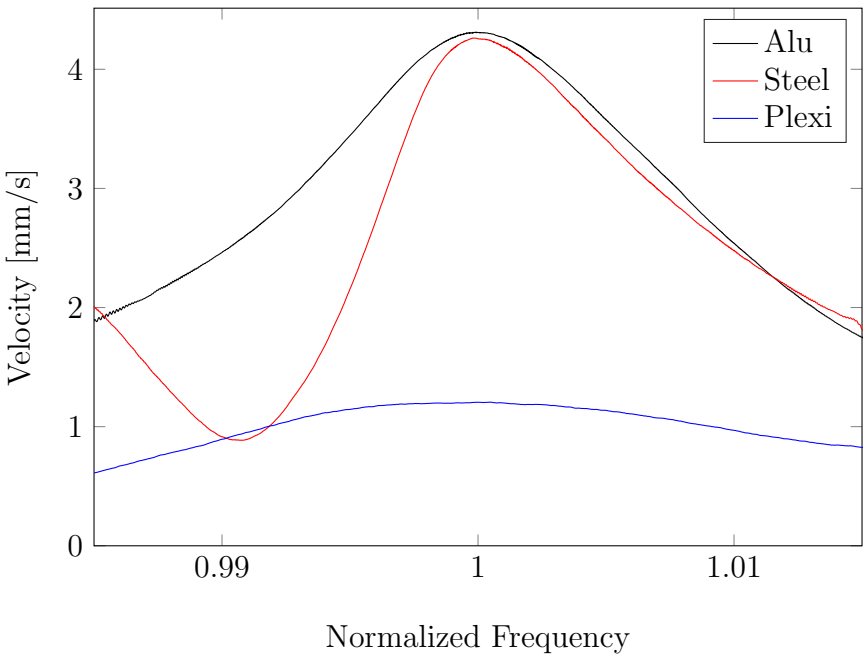

Figure 25: Resonance shape for different holder materials. Plexiglas has a high damping effect on the specimen.

proven if the resonance peak shape is compared, see Figure 25. For the plexiglas fixture the velocity response of the specimen at the same excitation amplitude is flatter and no clear resonance peak is formed. For the two other materials a clear resonance peak is formed which is really steep especially for the stainless steel holder.

Due to the high damping the frequency shift is disturbed at higher amplitude excitations and the extracted α gives no actual material property. In contrast, for the aluminum and stainless steel holder the slope is almost identical, this means for the same specimen at the same measurement point the same nonlinearity parameter α is measured. In following experiments no plexiglas fixture is used anymore as a result of their negative damping characteristics.

3.3.4 Couplant

The couplant is necessary to guarantee sufficient contact between the ultrasonic transducer and the specimen, in experiments without couplant a slower velocity response

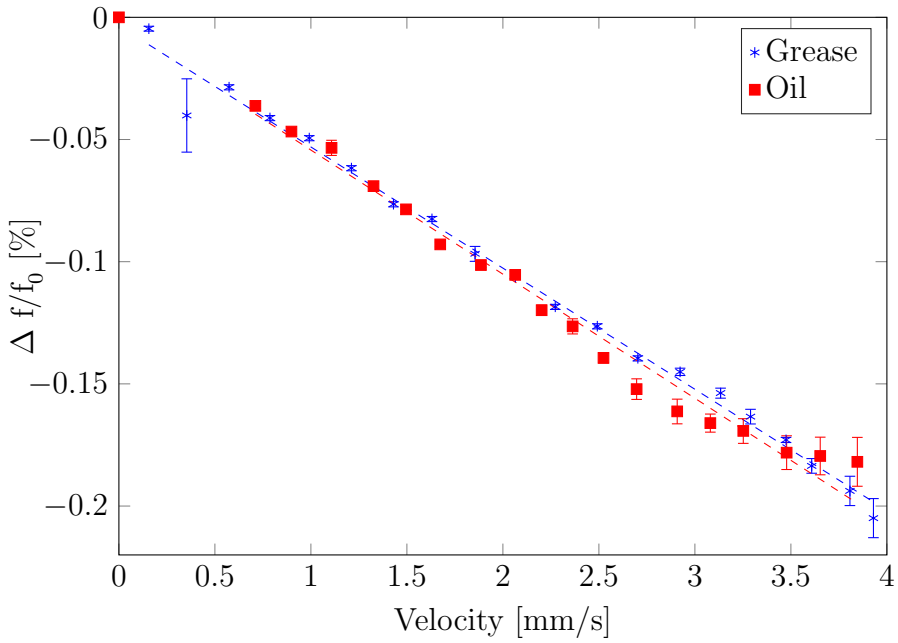

Figure 26: Frequency shift for the same material with different couplants.

is observed. The transducer surface around the contact point is coated with couplant to improve the wave transmission. To validate the couplant influence vacuum grease and oil are used and α is compared for two measurements at the same specimen. As shown in Figure 26, the relative frequency shift is independent of the couplant, thus the nonlinearity parameter α is the same.

3.3.5 Sweep Time

To check the influence of excitation duration the nonlinearity parameter α for the same sample at the same force is analyzed for different sweep times. This means the duration in which the frequency is changed between the lowest and the highest frequency of the measurement frequency band is varied. As we can see in Table 2 the change in the nonlinearity parameter α due to the sweep time is small. For the further measurements a sweep time of 2 s is chosen.

Table 2: Nonlinearity Parameter for different Sweep Times

Sweep Time	α
1 s	-0.08104
2 s	-0.07745
3 s	-0.07828
4 s	-0.07998
5 s	-0.08079
6 s	-0.08320

3.4 Repeatability of NRUS Measurements

To check the repeatability for the setup a specimen is measured five times. In between the measurement runs, the specimen is unmounted and remounted to the fixture, wherefore small changes in the position of the specimen in the fixture can be present. Besides, the amount of couplant couldn't guaranteed to be identical for every measurement. The force acting on the specimen is set constant and the same holder is used. Figure 27 shows the normalized difference of each measurement run from the mean of these 5 measurement runs. The maximal deviation from the mean is 5.5 % for the first measurement, which is an acceptable value for this type of measurement and confirms the reliability of the measurement procedure. In general, the repeatability with the developed experimental setup is small enough to detect microstructural changes as shown in Chapter 5.

3.5 System Nonlinearity

As started to discuss in section 3.3.1 there are potential nonlinearity sources besides the microstructure of the specimen. As seen in Figure 21 the transducer itself is a source of nonlinearity and shows a frequency shift for stronger excitations. This amount of frequency shift introduced by the piezoelectric transducer increases with increasing excitation voltage. Another source of nonlinearity is the measurement setup and the post-processing, as discussed previously in section 3.4 changes up to 10 % are due to changes in the contact condition or uncertainties in the peak detection. We can

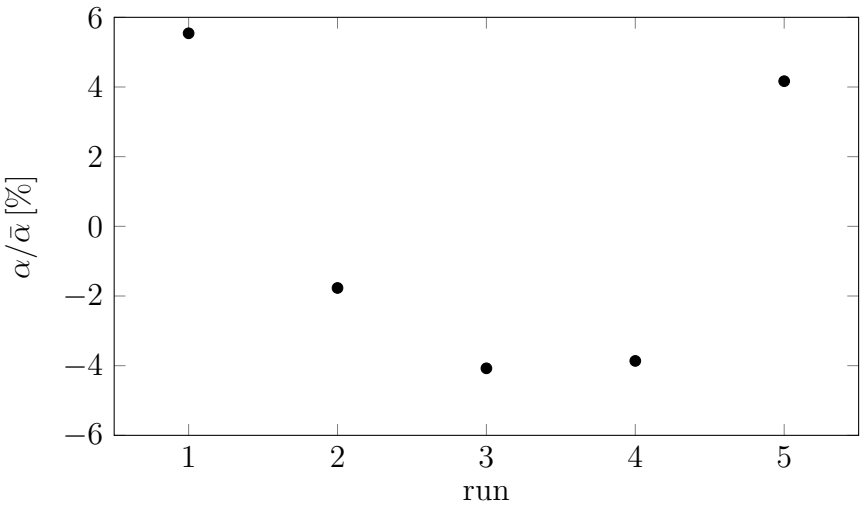

Figure 27: α for different measurement runs.

therefore conclude, that a measurement of the material nonlinearity parameter, using an increasing input voltage to excite the resonance mode with different amplitudes is only valid as long as the transducer and system nonlinearity is neglectably small compared to the second harmonic generation due to material nonlinearity.

Figure 28 gives a qualitative expression of the contributions of the system, the transducer and the material. The dashed line shows the measured transducer nonlinearity and can be estimated as constant for all measurements. The dotted line is a schematically expression of the system nonlinearity and varies for every measurement. Based on the in Section 3.4 shown results, their influence is significantly smaller than the material nonlinearity. The solid line and the marks are the measurement results for Al1100. In general, aluminum is known to have a very low nonlinearity compared to stainless steel [10].This means for other materials, and especially for the stainless steel used to analyze the influence of thermal damage, the slope of the line will be steeper. As a result, the signal to noise ratio between material and other nonlinearities will be higher than for this specimen. Consequently, the developed setup is useful to measure the material nonlinearity.

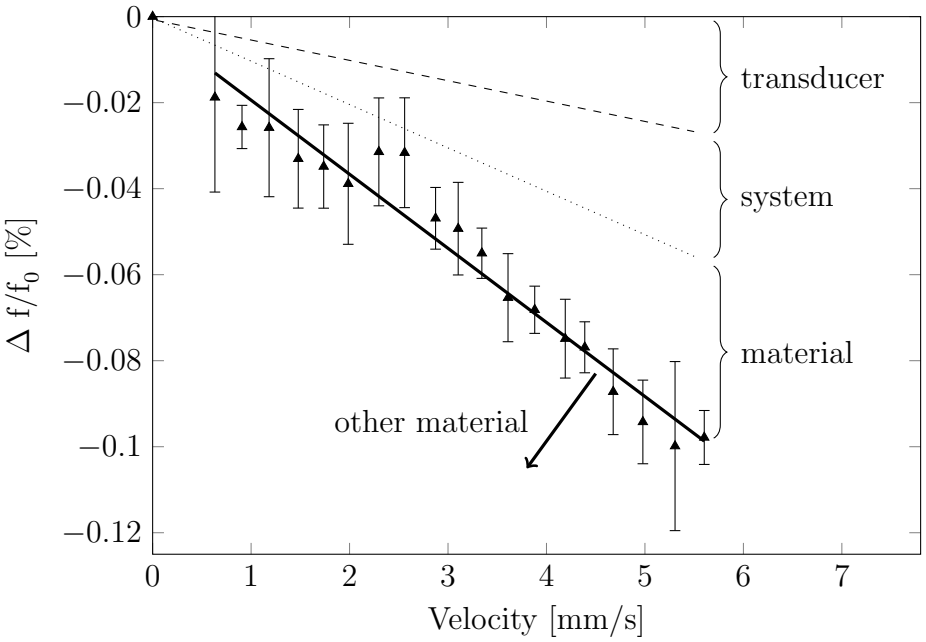

Figure 28: Resonance frequency shift for Al1100 over different peak velocities; the dashed line represents the measured transducer nonlinearity and the dotted line the summation of both a potential system nonlinearity and the contribution of transducer nonlinearity.

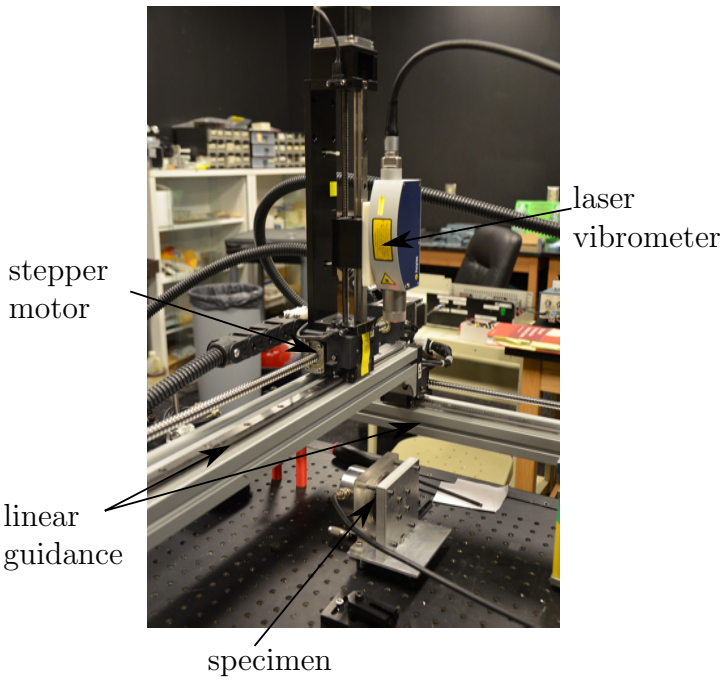

Figure 29: Automatic scanning stage to perform grid measurements.

3.6 Grid Measurement

To visualize the resoance mode shape of the sample a grid measurement over the whole sample geometry is done. For this purpose, a automatic scan stage is used which allows the movement into two direction in space. Figure 29 shows the scan stage with the mounted laser vibrometer which is moved by two stepper motors. The automatic stage is controlled using a LabVIEW program. The stage scans the whole specimen with a grid spacing of 1 mm. The resonance response for different driving amplitudes is scanned in each point. Afterwards the laser vibrometer moves to the next measurement point.

The upper part of Figure 30 shows the velocity at the corner opposite to the transducer – the lower corner in the plate illustrations. This point represents the measurement point for the measurement of the hysteretic nonlinearity parameter α, because there the highest velocity is measured. The picture one to four show the velocity distribution for the whole plate at the different frequencies. For the

first frequency at 34.7 kHz the plate has just little movement, but for a frequency closer to the resonance one clearly see how the velocity increases and a symmetrically distribution can be seen. A similar mode shape can also be observed if the situation in 2 and 4 is compared. These two measurement points are below and above the resonance peak frequency at the approximately same velocity response and show a similar velocity distribution on the surface of the specimen.

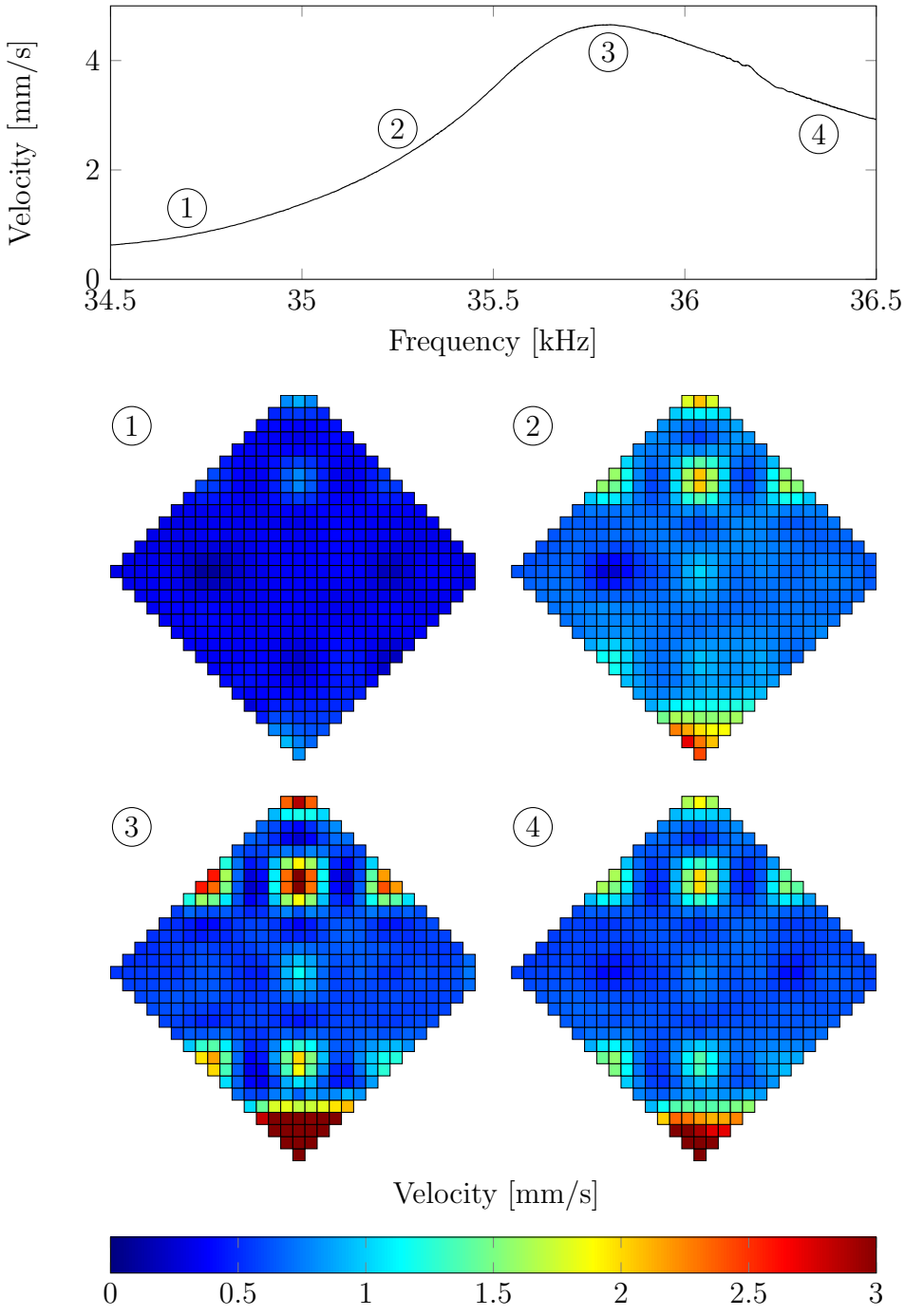

Figure 30: Visualized mode shape at different frequencies. The color represents the measured vertical out of plane velocity on the surface.

CHAPTER IV

MATERIAL ANALYZED

Previous research [20] has shown that second harmonic generation is feasible to detect microstructural changes in reactor pressure vessels (RPV). Instead of using difficult to handle irradiated samples, 17-4PH stainless steel can be used because it shares some features in the microstructure with irradiated RPV. During thermal aging of 17-4PH stainless steel, copper-rich precipitates are formed which increase the hardness of the material. According to [27] RPV steels are subjected to neutron irradiation experience the growth of copper-rich precipitates which have the highest contribution on the radiation embrittlement. This chapter provides background information on 17-4PH stainless steel, the sample preparation and thermal aging procedure. Finally, this chapter introduces the measurements for the nonlinearity parameter β performed in [19] and [20] which were used to quantify the influence of precipitates formation during thermal aging of 17-4PH stainless steel on the acoustic nonlinearity.

4.1 Material Properties of 17-4PH Stainless Steel

17-4PH stainless steel is a martensitic alloy which is precipitate-hardenable therefore, it provides a good combination of strength, corrosion resistance and mechanical properties which is why it is widely used for several engineering applications. 17-4PH transforms from austenite to martensite phase irrespective of the cooling rate as soon as the temperature drops below 160°C. Thermal aging of the material in a temperature range between 400°C and 600°C leads to hardening of the material [24]. Precipitates are formed, because the solubility of copper is low in this temperature range, as a result of which these atoms are forced to the grain boundary and produce fine particles. These precipitates impede the movement of dislocations throughout

the lattice, this serves to harden the material. Up to a peak aging time the precipitates are growing and coincidently the hardness of the material is increased. Above this peak aging time the structure is weakened because the precipitates are too big to form a coherent structure in the matrix. Hsiao et al [11] showed, that the size of these copper-rich precipitates for a sample that was aged for 1 hour at 480°C, after solution annealing and water quenching, is between 15 nm and 25 nm. Whereas, Murayama et al. [25] reported diameter of 3 nm after 100 hours of aging at 400°C, and a diameter of 8 nm after 5000 hours of aging at 400°C. In the solution annealed state 17-4PH has mainly a martensitic structure apart of ≈7% alpha-ferrite [3]. Christien et al. [3] reported that the dislocation density in the martensite at room temperature is at $4 \times 10^{15}/m^2$, and about $1 \times 10^{15}/m^2$ in the austenitic phase and remains constant up to about 500°C. The formation of dislocations occurs during the martensite to austenite transformation, due to the difference in density of the two phases such that regions of forming martensite cause deformation on the surrounding austenitic regions. It is known that dislocations affect the nonlinearity of the material, and this study aims to study the effect of only the precipitates on the nonlinearity. As a result the thermal aging time for 17-4PH must be below 500°C where the dislocations density is known to be constant.

4.2 Sample Preparation

One objective of this research is to compare the results of the acoustic nonlinearity parameter β with the results for the nonlinearity parameter α, therefore the exact same samples are used as in [19]. The 17-4PH stainless steel, composition in Table 3, has a tensile strength of 1384 N/mm^2 and a yield strength of 1263 N/mm^2. Before the heat treatment, the as-received material is solution annealed at 1040°C for 6 hours, and then air cooled. The raw geometry is used for bar samples with a dimension of 19 mm x 38 mm x 230 mm, besides some Charpy samples with geometry of 10 mm x

Table 3: Composition of 17-4PH stainless steel as received

C	Cr	Cu	Ni	Mn	Si	Nb
0.023	15.15	3.07	4.46	0.63	0.46	0.26
Mo	Co	N	P	S	Ti	Fe
0.08	0.044	0.023	0.016	0.001	0.001	rest

10 mm x 56 mm are cut using wire EDM. The Charpy sapmples are not from the same batch than the bar samples, wherefore an identical composition of the material can not be guaranteed. All specimens are surface ground after the solution annealing and cooling at at low speed and with sufficient cooling to ensure smooth surfaces which are necessary for the second harmonic measurements.

The bar samples are aged at 400°C for 0.1h, 1h and 6 hours to compare several precipitation stages of the material based on the hardening experiments of 17-4 PH stainless steel reviewed by Mirzadeh et al. [24] ("AC"-samples).

Two bars are used to create a reference condition therefore, these bars are annealed a second time at 1100°C for 2 hours in an uncontrolled atmosphere and afterwards water quenched ("WQ"-samples). This procedure produces a significant decrease in the hardness which can be seen in the comparison to air cooled samples as shown in Figure 31 and predicted in [11]. Further, one sample was then aged for 1 hour at 400°C to separate the aging effect after water quenching with the air cooled ones.

Similar to the bar samples, the Charpy samples are aged from the as-received state ("AC"-samples) for 1h and 6 hours. A second solution annealing treatment at 1175°C for 2 hours in a vacuum furnace, and subsequently quenched with high-pressure gas ("GQ"-samples) is given to three other specimens. The second solution annealing and protective gas quenching prevents precipitation formation during cooling, so that we assume that these samples are free of precipitates. Afterwards two of them are aged for 1 and 6 hours.

All specimens are aged in an uncontrolled atmosphere and heated in a furnace from room temperature at an average rate of 9°C/min. A thermometer is used to

Table 4: Overview of the different samples and their heat treatment procedure after solution annealing.

Reference Geometry	Sample Designation	Cooling	Heat Treatment
bar	WQ	water quenched	-
	WQ-1	water quenched	1h
	AC	air cooled	-
	AC-0.1	air cooled	0.1h
	AC-1	air cooled	1h
	AC-6	air cooled	6h
Charpy	GQ	gas quenched	-
	GQ-1	gas quenched	1h
	GQ-6	gas quenched	6h
	AC	air cooled	-
	AC-1	air cooled	1h
	AC-6	air cooled	6h

control the temperature at the surface of the specimen. After the heat treatment all samples are air cooled to room temperature. A overview of all samples and their heat treatment conditions is given in Table 4.

For the NRUS experiments the samples are cut into 10 mm x 10 mm x 2 mm slices by using a wire EDM, which allows a high precision without influencing the mechanical properties of the material. During the EDM cutting process the whole sample is completely submerged in a tank of cooling fluid and a low cutting speed is used, so the thermal induced stresses are low. Finally, all samples are hand polished with 250, 400, 800, 1500 and 2000 grit polish paper to receive a reflective surface, which is necessary for laser vibrometer measurements.

4.3 Sample Condition

In the next subsections, the condition of the samples before they are cut into slices, is presented.

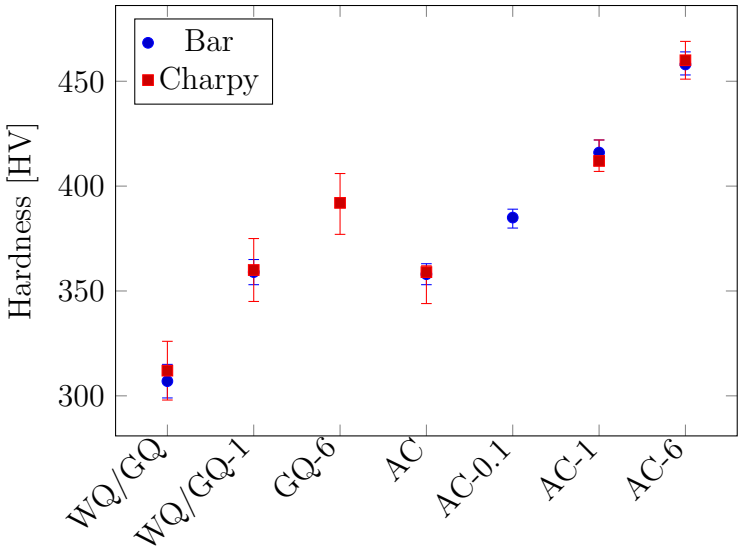

Figure 31: Vickers hardness of specimens analyzed.

4.3.1 Harndess

Vickers hardness measurements are performed [19],[33] on all samples after thermal aging. A Buehler High Quality Hardness Tester is used at a load of 2000g or 19.613N, which is applied for 10s, at twelve individual measurement points, six of them along the length of the sample, six along the width. The given Vickers hardness in Figure 31 represents the average of these 12 measurements to consider anisotropic effects.

Obviously the hardness is increasing with thermal aging time as shown in Figure 31 – this behavior is also described in [24]. In general it can be concluded that the increase in hardness is proportional to the density and size of coherent precipitates, which reduces the mobility of dislocations. Further, the hardness of the water/gas quenched samples is significantly lower than for the air cooled samples due to the higher cooling rate. Quenching disturbs the diffusion of copper to the grain boundary and so less precipitates nucleate.

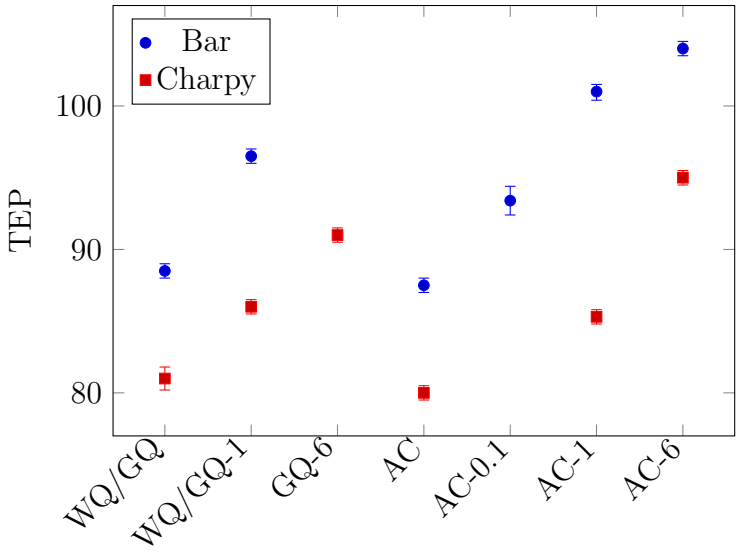

Figure 32: Thermo-electric power measurement results of specimens analyzed.

4.3.2 Thermo-Electric Power Measurement

The Thermo-electric power measurement (TEP) is based on the Seebeck effect, which predicts a ΔV along a temperature gradient ΔT across the sample. The change in the voltage is very sensitive to the chemical composition. The TEP value increases due to coherency strains of precipitates, and decreases due to dislocations. Incoherent precipitates have no effect on the TEP value. The measurements are done on a Koslov Thermo-Electric Alloy Sorter TE-3000, which has to be calibrated with a Hastelloy C-276 steel probe. The sample surface is cleaned using acetone to remove all residues. In general, the TEP measurement is independent of the sample geometry and delivers results instantly. Up to five measurements are done on each heat treated sample at different locations to obtain a representative value. As for the hardness, the TEP value is increasing with the thermal aging time as shown in Figure 32. This increase is caused by the increase in the density of copper rich precipitates which leads to a decreasing amount of copper in the matrix material. The bar samples show for all conditions a significantly higher TEP value when compared to the Charpy samples, which supports the assumption that the composition of these two material batches is

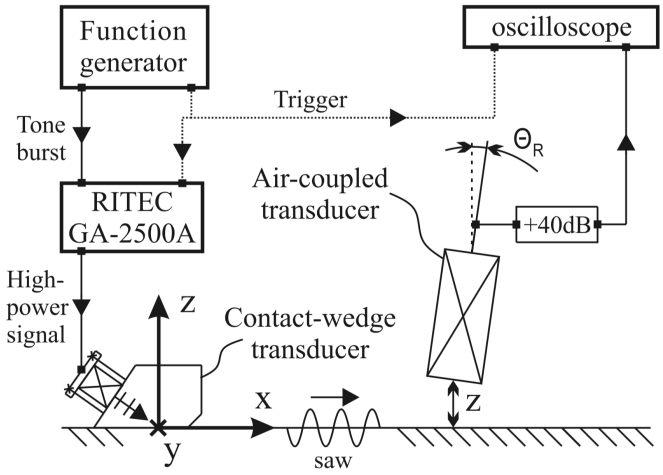

Figure 33: Sketch of experimental setup for Rayleigh wave SHG measurements from Thiele et al. [34]

different.

4.3.3 β-Measurements

Figure 33 shows the Rayleigh wave measurement setup used as described in [34] to measure β in the bar samples. A tone burst at 2.1 MHz is generated by function generator and then amplified. A piezoelectric transducer excites a longitudinal wave, which is transformed into a Rayleigh surface wave by an acrylic wedge. At different propagation distances an air coupled transducer, with a center frequency close to the second harmonic of the source frequency, is placed above the specimen, to receive the longitudinal wave leaked into the air by the Rayleigh surface wave. With increasing propagating distance the value of the second harmonic A_2 increases, due to the material nonlinearity of the specimens.

In the post processing, an FFT of the windowed signal is processed and the amplitudes of the first (A_1) and second harmonics (A_2) for each propagating distance are extracted. A linear regression between A_2/A_1^2 and the propagation distance is performed – see Thiele et al. [34] for details. The slope of this $A_2/(A_1)^2$ fit is proportional to the acoustic nonlinearity parameter β.

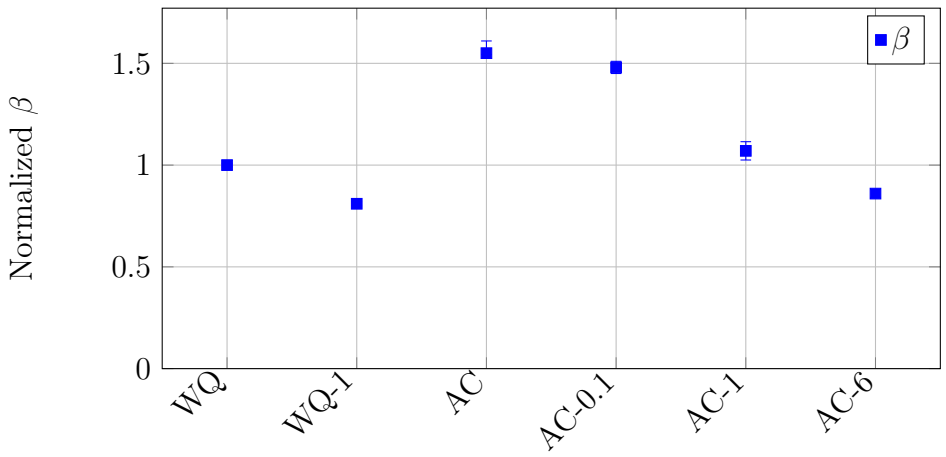

Figure 34: Normalized relative nonlinearity parameter β obtained by nonlinear Rayleigh wave measurement using air-coupled receiver

Table 5: Normalized measured β for water quenched and air-cooled bar samples

Sample Condition	$\Delta\beta/\beta_{\text{no HT}}$
WQ	0 %
WQ-1	-19%
AC	0 %
AC-0.1	-8%
AC-1	-34%
AC-6	-47%

The normalized β-measurement results for the bar samples at different thermal aging conditions are shown in Figure 34. In Table 5 the change relative to the state before the heat treatment is compared. Clearly a decrease in β with increasing heat treatment is observed as explained in [20] therefore, the Rayleigh wave measurement setup is sensitive to detect changes in the microstructure triggered by the heat treatment.

To measure the Charpy samples, Rayleigh surface waves can not be used because of the short propagation path, so instead longitudinal waves are used. Two small piezoelectric contact transducers are mounted on opposite sides as shown in Figure 35. Again the second harmonic of the Hann windowed FFT are obtained, but instead of varying the propagation distance, the amplitude of the exciting transducer

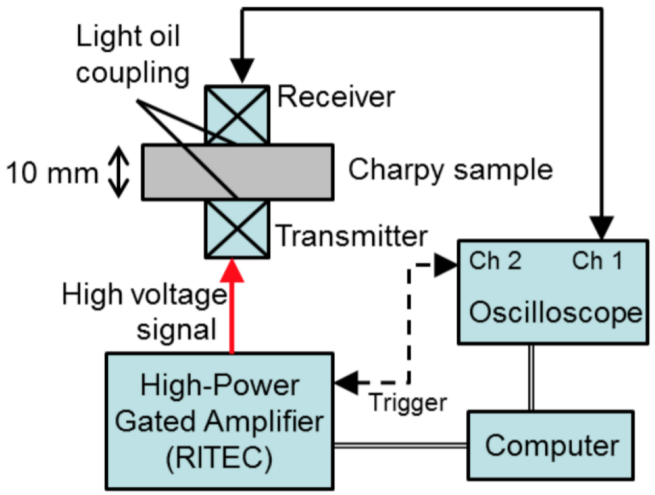

Figure 35: Sketch of experimental setup for longitudinal SHG measurements from Matlack et al. [22]

is incrementally increased. The slope of the linear regression between A_2 and A_1^2 of different excitation levels, is a relative measure of the acoustic nonlinearity parameter and proportional to β. For details regarding the longitudinal wave measurement setup and its post processing see [22].

Table 6 shows the results in the change of β normalized to the untreated state for Charpy samples. The standard derivation and the average change in the different specimens is given. No significant changes in β due to aging at either 1 or 6 hours can be observed. A slight increase in β is detected, but the standard deviations are on the same order of magnitude. Wherefore, longitudinal wave measurements of β are less sensitive than Rayleigh wave measurements. As a consequence, there is a lack of methods to detect microstructural changes in small specimens using nonlinear second harmonic generation ultrasonic techniques.

Table 6: Normalized measured β for gas quenched and air-cooled Charpy samples

Sample Condition	$\Delta\beta/\beta_{\text{no HT}}$	Standard Deviation
GQ-1	+4.9%	3.7%
GQ-6	+3.4%	2.4%
AC-1	+6.6%	5.9%
AC-6	+0.7%	12.3%

CHAPTER V

NRUS RESULTS

This chapter presents the results for the measured hysteretic nonlinearity parameter α. The material preparation and its condition is given in the previous chapter. Figure 36 presents the results of the solution annealed and air cooled bar samples. Each data point represents one measurement at a certain excitation amplitude. For each excitation amplitude, 9 separate sweeps on the same specimen without changing the position of the laser or any other parameters are recorded. The error bars indicate one standard deviation from the mean of these 9 sweeps. The dashed line gives the linear fit between the normalized frequency shift over measured velocity, and the slope of this linear fit is the value α. The exact values and the relative decrease from the unaged condition of α are shown in table 7 .

One can clearly see the decrease in nonlinearity with increasing heat treatment time for the air cooled samples. The increase in volume fraction of precipitates, as seen in the TEP measurements, yields to a stiffening of the structure. This supports the assumption that precipitates impede the movement of the dislocations, because the dislocation density is constant for this material. The decrease between the unaged sample (AC) and the one which is heat treated for 6h (AC-6) is quite significant – there is a more than 70% decrease between these two chemically and geometrically identical samples, whose only difference is the formation of precipitates. Hence, it can be concluded that the proposed ultrasonic resonance spectroscopy setup is very sensitive to the mircostructural changes associated with precipitates. For a short heat treatment time of 0.1h, the drop in α is only -11%, but for a thermal aging time of 1h the drop is already more than –50% compared to the untreated reference

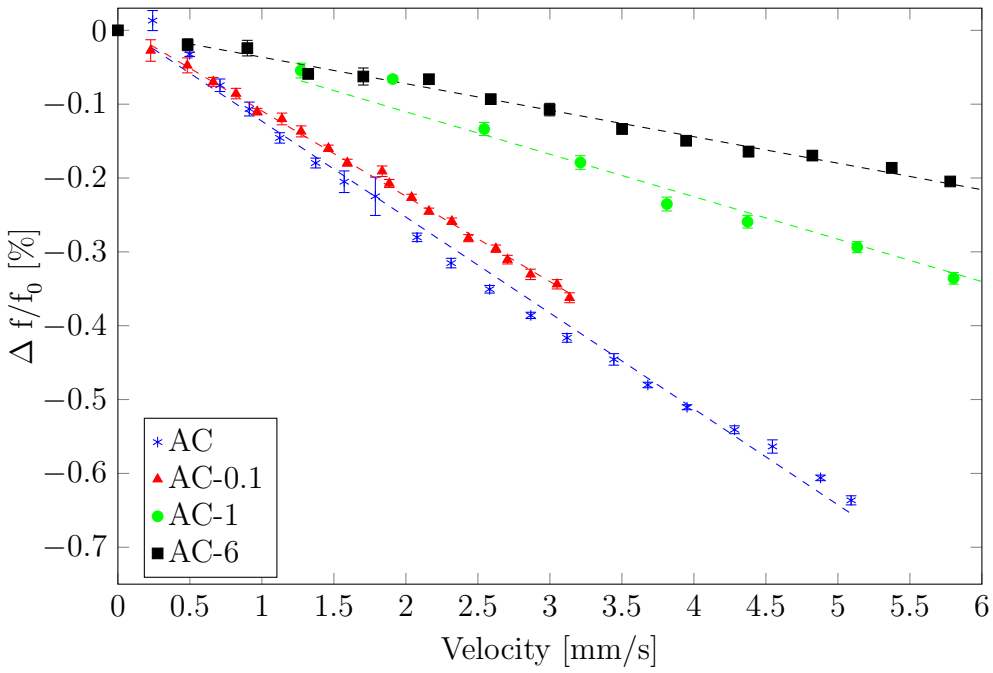

Figure 36: Measurements of the frequency shift for air cooled thermally aged 17-4PH bar samples.

condition. This means after 1h of thermal aging, there is already a significant amount of precipitates formed, which prevent the movement of dislocations. This assumption is underlined by the fact that the relative change between 1h and 6h is small compared to the previous one. It seems that saturation effects occur after 1h of aging.

Figure 37 shows the results for the water quenched samples (WQ) as well as for a reference piece of Al1100. The aluminum 1100 has a much lower nonlinearity parameter α than untreated stainless steel. This supports the results presented by Haupert et al. [10]. Like in air cooled specimens, the heat treated specimen shows an increase compared to the untreated one of –29%. For the air cooled specimens the the relative change after one hour at 400°C is –55%, the difference in the change may be explained that during the cooling for the air cooled samples precipitates are still formed due to the lower cooling speed. The purpose of the water quenched specimen is to create a baseline condition in which precipitation formation during cooling from

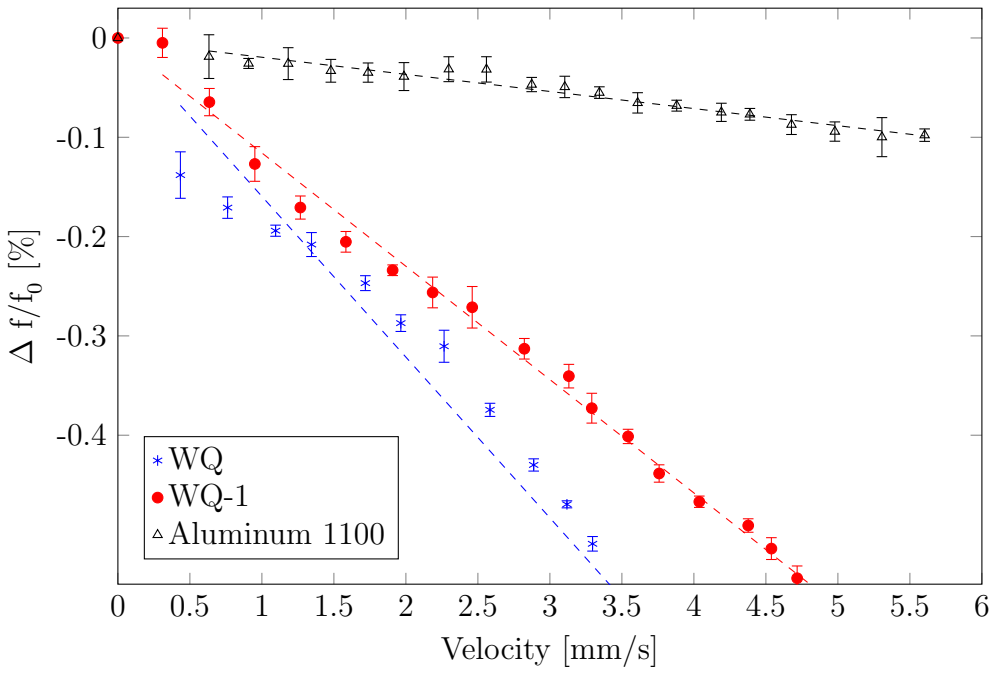

Figure 37: Measurements of the frequency shift for water quenched thermally aged 17-4PH bar samples and aluminum 1100.

the solution annealing is avoided.

Figure 38 shows all measured α values are normalized to the one measured for the water quenched specimen. A decrease in nonlinearity observed from the WQ sample to the AC sample can be seen, which is reasonable since the water quenching should prevent the formation of copper rich precipitates, and therefore the movement of the dislocations is not impeded by precipitates. The difference between these two specimens of about 19% is due to the precipitates formed at the slow cooling in air.

Table 7: Measured nonlinearity parameter α for 17-4PH bar samples thermally aged material at 400°C in water quenched and air cooled state.

Sample Condition	α	$\Delta\alpha/\alpha_{\text{no HT}}$
Air cooled no HT	–0.12989	0%
Air cooled 0.1h @400°C	–0.11557	–11%
Air cooled 1h @400°C	–0.05748	–55%
Air cooled 6h @400°C	–0.03589	–72%
Water quenched no HT	–0.16186	0%
Water quenched 1h @400°C	–0.11412	–29%

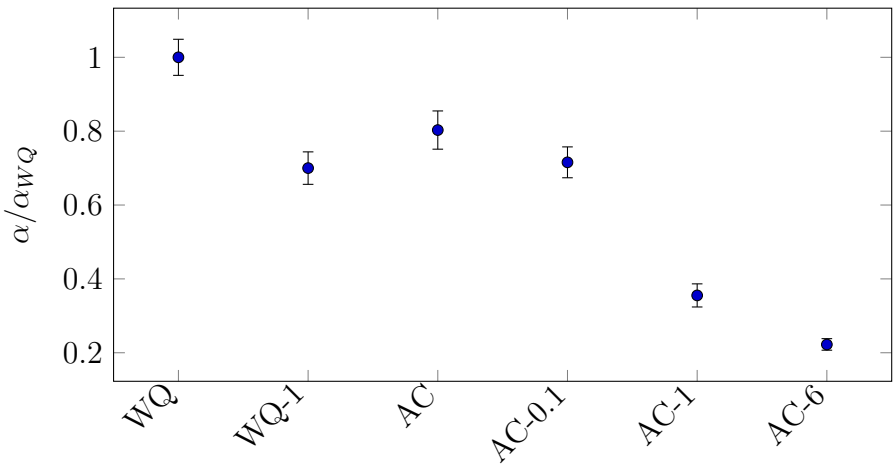

Figure 38: Normalized measured α for 17-4PH thermally aged material at 400°C compared to water quenched state bar samples.

Results for the specimen cut from the Charpy specimen are shown in Figures 39 and 40. Measurements of the untreated condition are compared to those of the heat treated condition. For the air cooled specimens, a decrease of the nonlinearity parameter α between the untreated and the heat treated specimen is measured. However, there is an unexpected increase between the 1h and 6h heat treated specimens. To rule out some random damage in the specimens used another slice out of the Charpy should be cut out – for this measurements only one slice of each specimen was used. Except for the 1h heat treated specimen the α values, of the samples cut of the Charpy specimens are lower than for the bar specimens presented before. Note that, the same material is used and the same thermal aging procedure is applied for each case. But, as we have seen in Figure 32, the TEP values between both geometries are different, therefore the assumption of a identical specimen composition is not valid. This is why the results of bar and Charpy samples can't be directly compared, and we can only focus on the relative change within each origin geometry. For the gas quenched samples the nonlinearity parameters α and their decrease compared to the

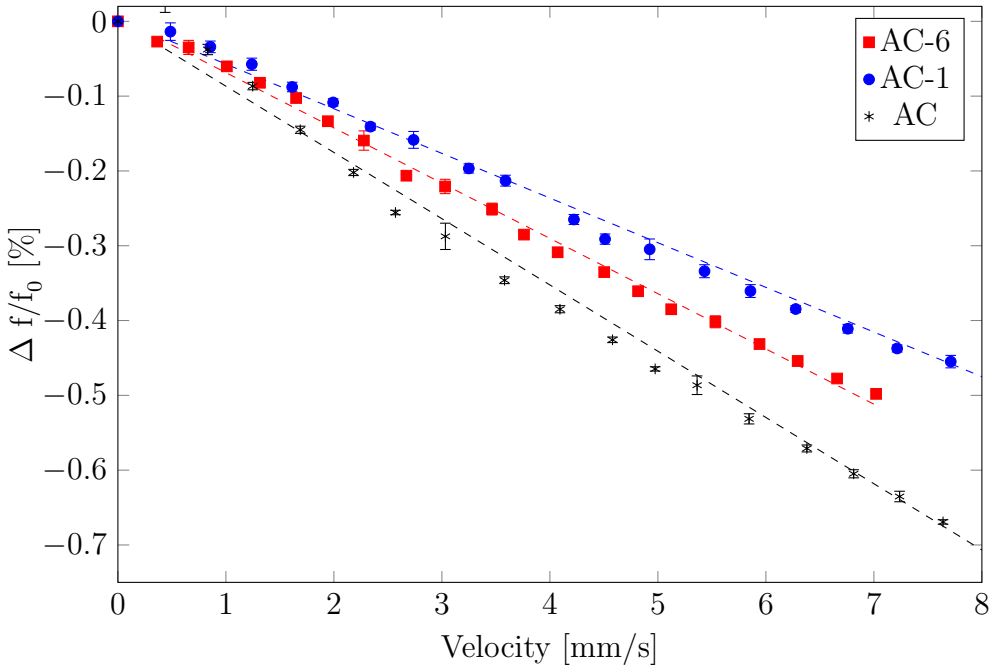

Figure 39: Measurements of the frequency shift for air cooled thermally aged 17-4PH Charpy samples.

untreated specimen are shown in Table 8. Again for the heat treated specimen, a decreasing resonance frequency shift is measured, which supports the assumption that precipitates impede the movement of the dislocations.

Table 8: Measured nonlinearity parameter α for 17-4PH Charpy samples thermally aged material at 400°C in gas quenched and air cooled state.

Sample Condition	α	$\Delta\alpha/\alpha_{\text{no HT}}$
Air cooled no HT	–0.08857	0%
Air cooled 1h @400°C	–0.05971	–32%
Air cooled 6h @400°C	–0.07387	–16%
Gas quenched no HT	–0.21289	0%
Gas quenched 1h @400°C	–0.14471	–32%
Gas quenched 6h @400°C	–0.06650	–69%

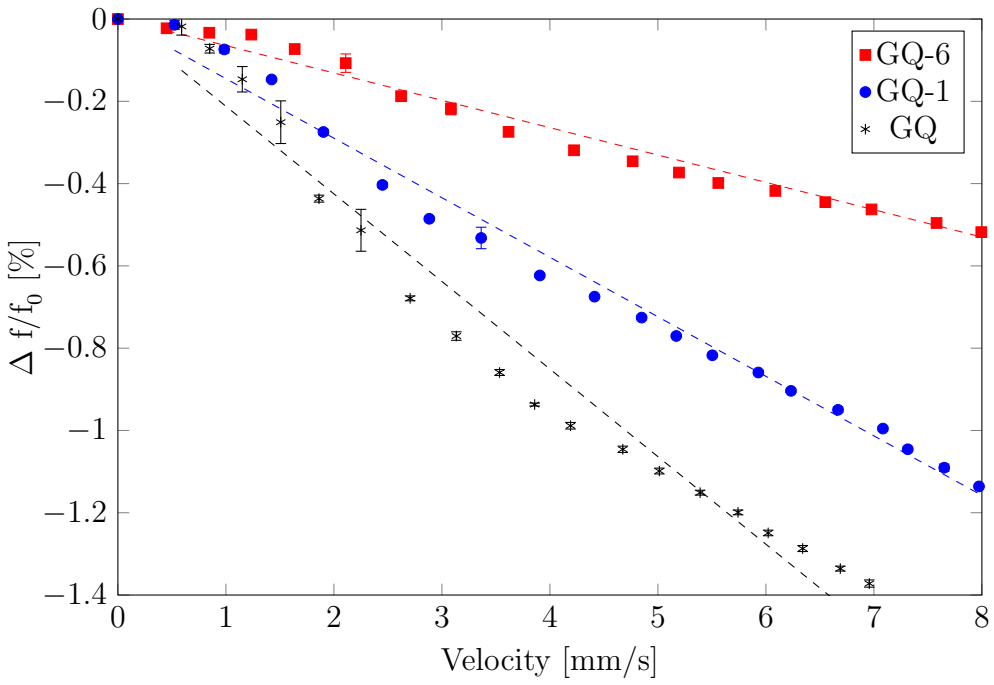

Figure 40: Measurements of the frequency shift for water quenched thermally aged 17-4PH Charpy samples.

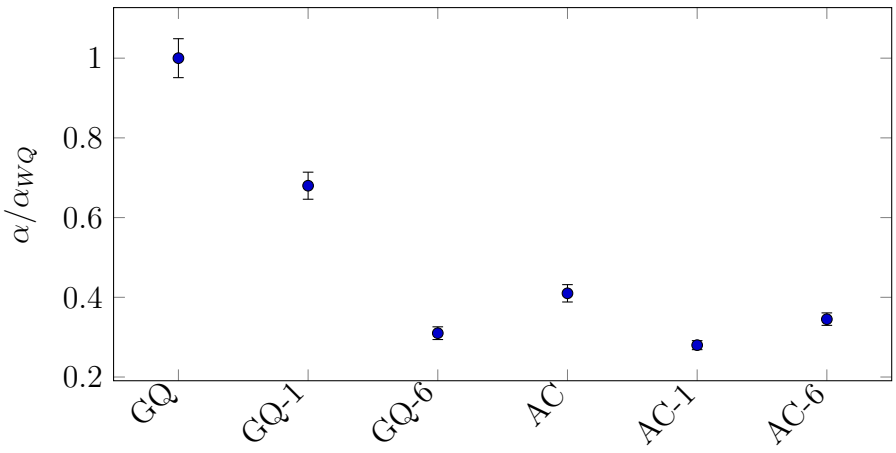

Figure 41: Normalized measured α for 17-4PH thermally aged material at 400°C compared to water quenched state Charpy samples.

CHAPTER VI

SENSITIVITY OF NRUS

This chapter comapred the sensitivity of nonlinear ultrasonic nondestructive evaluation methods. The results are separated according the geometry and the cooling procedure.

Figure 42 shows the relative frequency shift for different heat treatment times of the bar samples. The y-axis gives the α value normalized to the untreated AC sample. The β determined by Rayleigh wave second harmonic generation as well as the NRUS results show a decrease with thermal aging time. For the AC-6 sample the value is 47 % lower than in the untreated condition, whereas the NRUS has a change of more than 70 %. The higher sensitivity with the NRUS when compared to the Rayleigh wave results can be observed for every heat treated specimen. Only for the 0.1h heat treated specimen the difference between β and α is relatively small. For this short thermal aging time the precipitates are small, and therefore their ability to impede dislocation motion is small. The same trend is observed for the water quenched specimens in Figure 43, again the α measurement is more sensitive to indicate microstructural changes due to precipitation.

For both measurement methods the relative change is higher for the air cooled specimens than for the water quenched. For a thermal aging time of 1h, the relative change of α in the air cooled specimen is –55 % and for the water quenched specimen –29 %. In the β-measurements for air cooled the relative change is –34 % and for the water quenched specimen –19 %. This effect might be caused by the initial larger precipitates size in the air cooled samples – before heat treatment. These larger precipitates grow fast due to their larger surface area, which effects both measured

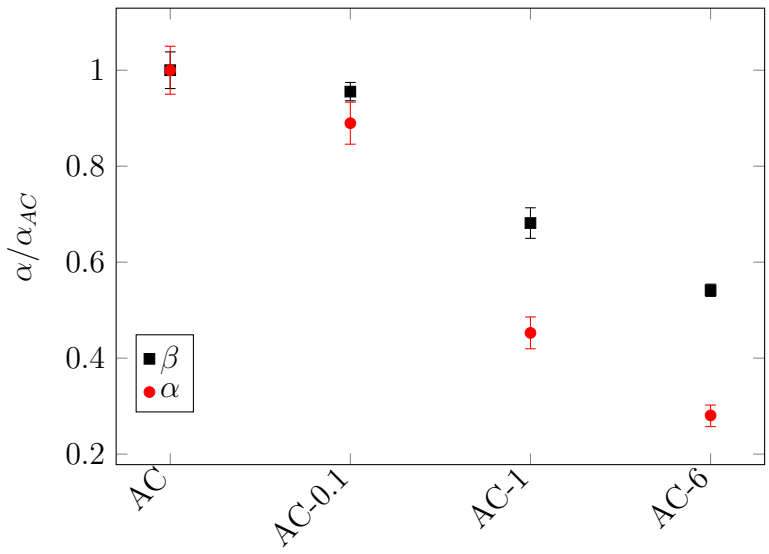

Figure 42: Comparison of nonlinear ultrasonic measurement of α and β normalized to the untreated air cooled specimen for the bar samples.

nonlinearity parameters, α and β. Additionally, Figure 44 shows a relative comparison normalized to the water quenched state.

Figure 45 and 46 present the trend for the Charpy samples. As mentioned in the previous chapter the decreasing trend of α with increasing thermal aging can't be confirmed, since the AC-6 specimen shows a higher α than the AC-1 specimen. However, a change in the nonlinearity α compared to the untreated specimen is detectable. In contrast to this,a decreasing α with increasing thermal aging time is determined for the gas quenched specimen. In the β measurement results for the second harmonic generation of a longitudinal wave no trend at all can be identified. In addition, the standard deviation within the measurements is large for the air cooled specimen. As mentioned in Chapter 4, the higher harmonic generation technique is not capable to detect changes in the microstructure for small specimen. The geometric limitations in these small specimens greatly restrict applications of propagating wave nonlinear ultrasonic techniques. However, for the NRUS technique, changes in the microstructure due to precipitation can be detected, which makes it a valuable tool

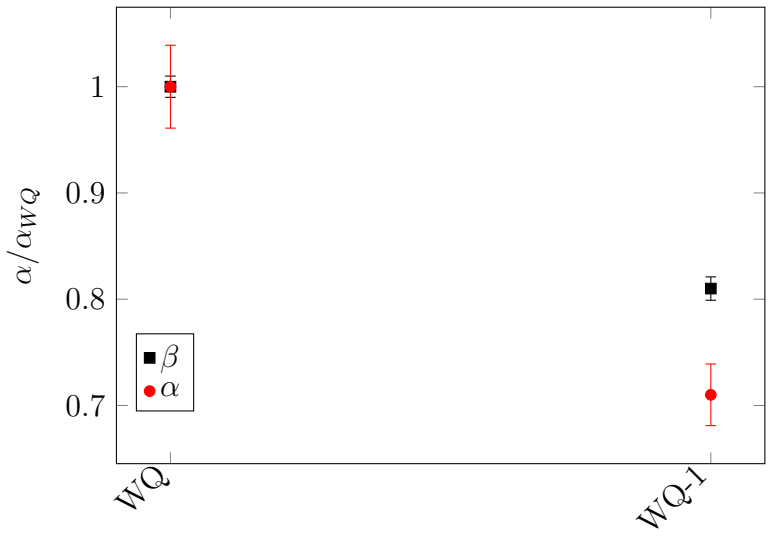

Figure 43: Comparison of nonlinear ultrasonic measurement of α and β normalized to the untreated water quenched specimen for the bar samples.

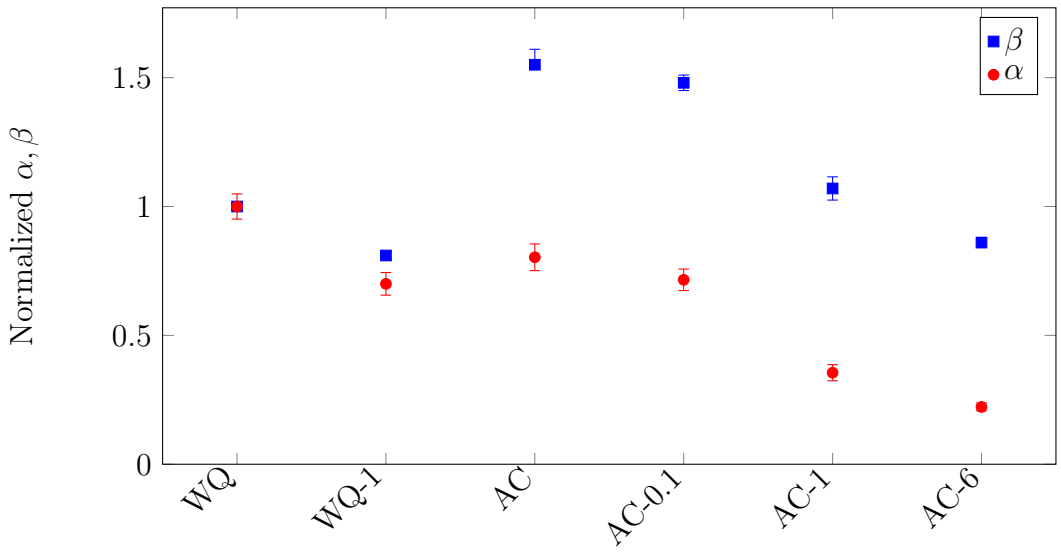

Figure 44: A complete comparison of all the results normalized to the water quenched state.

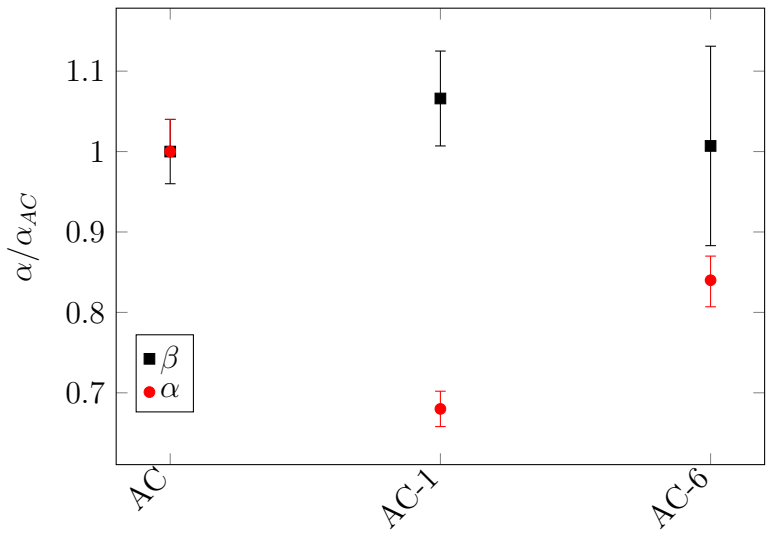

Figure 45: Comparison of nonlinear ultrasonic measurement of α and β normalized to the untreated air cooled specimen for the Charpy samples.

to close the gap of missing nonlinear ultrasonic measurements techniques for small specimens.

Finally, complementary methods like the hardness and TEP measurement are compared to the nonlinear ultrasonic techniques. Figure 47 shows that nonlinear methods are more sensitive than these complementary methods. Therefore, nonlinear methods are a valuable tool to characterize microstructural features in materials. In particular, the NRUS setup developed is able to detect these features in small specimens, which simplifies the measurement procedure for irradiated samples.

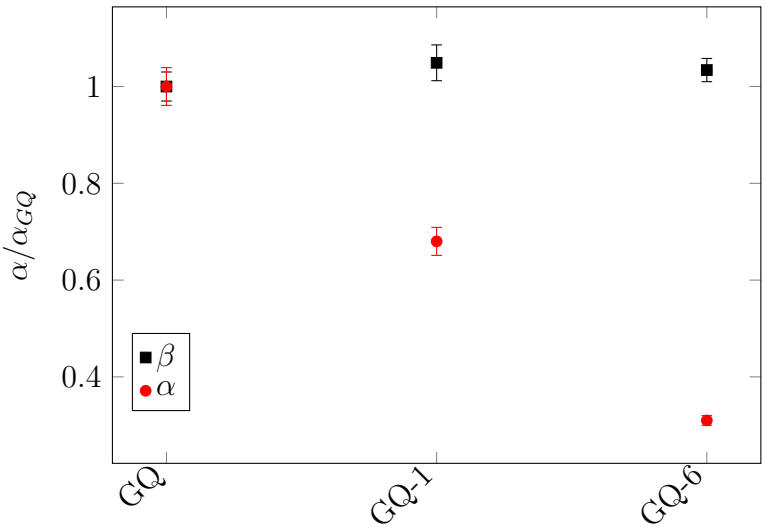

Figure 46: Comparison of nonlinear ultrasonic measurement of α and β normalized to the untreated gas quenched specimen for the Charpy samples.

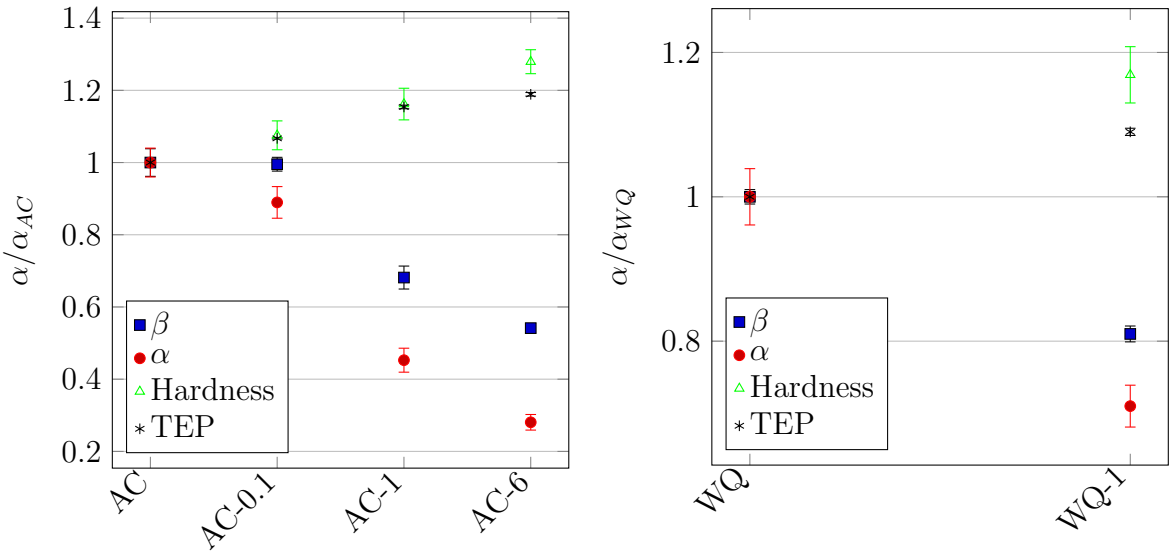

Figure 47: Comparison of linear and nonlinear methods towards their capability to detect precipitation.

CHAPTER VII

CONCLUSION

This research develops an experimental setup for the nonlinear ultrasonic spectroscopy (NRUS) procedure for small specimen and shows its accuracy, repeatability and sensitivity. The experimental setup and signal processing developed are capable of monitoring the excitation-amplitude dependent shift in the resonance frequency. System and non-material nonlinearity are determined in a procedure that separates these effects from the material nonlinearity. Therefore, the influence of the loading pressure, fixture material, couplant, and the sweep time are carefully analyzed. In addition, the inherent nonlinearity of the transducer is also accounted for to improve the assessment of the material nonlinearity contribution. Aluminum 1100 is used as a linear reference material compared to stainless steel and qualitatively compared to literature data. A fully automatic grid measurements setup is used to describe the exact mode shape in the frequency range used. In addition, the nonlinearity parameter at different spots is compared.

A short overview of the theoretical background of precipitate hardening and its influence on microstructural interactions is provided, to help the reader understand those microstructural evolution during the thermal treatment, which the specimens of this research are exposed to. Further, the hysteretic behavior of pinned dislocations is discussed which are potentially responsible for the hysteretic stress strain behavior of the material analyzed. Finally, an analytical solution for a resonant bar underlying hysteretic effects is shown, and the dependency of the resonance frequency from the excitation amplitude is predicted.

In this research, 17-4 PH stainless steel specimens undergoing thermal aging for

different periods are used. The nonlinearity parameter α is influenced by the different heat treatment durations, when the copper elements in the martensitic microstructure cluster in different precipitation stages. The results suggest a decreasing hysteretic behavior in the early stages of precipitation, which is investigated by comparing a solution annealed and water or gas quenched specimen with a solution annealed and air cooled specimen. With increasing heat treatment time, a decreasing nonlinearity parameter α is observed – this effect might be mainly due to the reduction of the dislocation mobility. Thermo-electric power (TEP) and microhardness measurement data support the assumption of an increase in volume fraction of precipitates with heat treatment time, which are known to impede the dislocation movement.

The sensitivity of the NRUS method is compared to that of known second harmonic generation technique, performed on the same specimens in the uncut geometry using Rayleigh surface or longitudinal waves. A higher sensitivity of the proposed NRUS method is observed for this material, especially for the Charpy samples, where the geometric limitations greatly restrict applications of propagating wave nonlinear ultrasonic techniques, and the longitudinal wave measurement is not capable of detecting microstructural changes due to precipitation.

In a future work the fixture and the loading mechanism need to be redesigned to improve the repeatability of the measurements. For example, linear rail guides could be integrated to increase the position accuracy of the specimen. Moreover, the resonance ultrasonic spectroscopy (RUS) method should be applied to determine the elastic properties of the specimen and use them to simulate the strain in the specimen. This would enable an absolute measurement of α and comparison of the measurement results to the literature values, instead of just doing relative measurements.

On the material side, further work is needed to show how the frequency shift is influenced by precipitation after peak-aging, when precipitates start to loose coherency. It is not clear if the same effects occur as in the pre-peak stage or other hysteretic

effects from microcracks get dominant, and therefore α starts to increase.

A further development of the resonance frequency shift method can be done, by performing non-contact measurements, therefore laser impact excitation is suggested. The non-contact method would reduce the external influences and only the material nonlinearity is detected. Especially, for the small specimens the laser excitation can be valuable alternative, due to its limited energy supply.

REFERENCES

[1] Achenbach, J., *Wave propagation in elastic solids*, vol. 16. Elsevier, 2012.

[2] Barsoum, M. W., Radovic, M., Zhen, T., Finkel, P., and Kalidindi, S. R., "Dynamic elastic hysteretic solids and dislocations," *Physical review letters*, vol. 94, no. 8, p. 085501, 2005.

[3] Christien, F., Telling, M., and Knight, K., "Neutron diffraction in situ monitoring of the dislocation density during martensitic transformation in a stainless steel," *Scripta Materialia*, vol. 68, no. 7, pp. 506–509, 2013.

[4] Finkel, P., Zhou, A., Basu, S., Yeheskel, O., and Barsoum, M., "Direct observation of nonlinear acoustoelastic hysteresis in kinking nonlinear elastic solids," *Applied Physics Letters*, vol. 94, no. 24, p. 241904, 2009.

[5] Gliozzi, A., Nobili, M., and Scalerandi, M., "Modelling localized nonlinear damage and analysis of its influence on resonance frequencies," *Journal of Physics D: Applied Physics*, vol. 39, no. 17, p. 3895, 2006.

[6] Granato, A. V. and Lücke, K., "Theory of mechanical damping due to dislocations," *Journal of applied physics*, vol. 27, no. 6, pp. 583–593, 1956.

[7] Guyer, R., McCall, K., and Van Den Abeele, K., "Slow elastic dynamics in a resonant bar of rock," *Geophysical research letters*, vol. 25, no. 10, pp. 1585–1588, 1998.

[8] Guyer, R. A. and Johnson, P. A., "Nonlinear mesoscopic elasticity: Evidence for a new class of materials," *Physics today*, vol. 52, pp. 30–36, 1999.

[9] Guyer, R. A. and Johnson, P. A., *Nonlinear mesoscopic elasticity: the complex behaviour of rocks, soil, concrete*. John Wiley & Sons, 2009.

[10] Haupert, S., Renaud, G., Rivière, J., Talmant, M., Johnson, P. A., and Laugier, P., "High-accuracy acoustic detection of nonclassical component of material nonlinearity," *The Journal of the Acoustical Society of America*, vol. 130, no. 5, pp. 2654–2661, 2011.

[11] Hsiao, C., Chiou, C., and Yang, J., "Aging reactions in a 17-4 ph stainless steel," *Materials Chemistry and Physics*, vol. 74, no. 2, pp. 134–142, 2002.

[12] Jhang, K.-Y., "Nonlinear ultrasonic techniques for nondestructive assessment of micro damage in material: a review," *International journal of precision engineering and manufacturing*, vol. 10, no. 1, pp. 123–135, 2009.

[13] Johnson, P. A., Zinszner, B., and Rasolofosaon, P. N., "Resonance and elastic nonlinear phenomena in rock," *JOURNAL OF GEOPHYSICAL RESEARCH-ALL SERIES-*, vol. 101, pp. 11–553, 1996.

[14] Kim, J.-Y., Qu, J., Jacobs, L., Littles, J., and Savage, M., "Acoustic nonlinearity parameter due to microplasticity," *Journal of Nondestructive Evaluation*, vol. 25, no. 1, pp. 28–36, 2006.

[15] Kim, J.-Y., Jacobs, L. J., Qu, J., and Littles, J. W., "Experimental characterization of fatigue damage in a nickel-base superalloy using nonlinear ultrasonic waves," *The Journal of the Acoustical Society of America*, vol. 120, no. 3, pp. 1266–1273, 2006.

[16] Landau, L. D. and Lifshitz, E. M., *Course of theoretical physics, Theory of elasticity*. Pergamon Press Oxford, 1986.

[17] Marino, D., "Using nonlinear ultrasound measurements to assess the stage of thermal damage in modified 9%cr ferritic martensitic steel," Master's thesis, Georgia Institute of Technology, 2014.

[18] Martin, J. W., *Precipitation hardening: theory and applications*. Butterworth-Heinemann, 1986.

[19] Matlack, K. H., *Nonlinear ultrasound for radiation damage detection*. PhD thesis, Georgia Institute of Technology, 2014.

[20] Matlack, K. H., Bradley, H. A., Thiele, S., Kim, J.-Y., Wall, J. J., Jung, H. J., Qu, J., and Jacobs, L. J., "Nonlinear ultrasonic characterization of precipitation in 17-4ph stainless steel," *NDT & E International*, vol. 71, pp. 8–15, 2015.

[21] Matlack, K., Kim, J.-Y., Jacobs, L., and Qu, J., "Review of second harmonic generation measurement techniques for material state determination in metals," *Journal of Nondestructive Evaluation*, vol. 34, no. 1, pp. 1–23, 2015.

[22] Matlack, K., Wall, J., Kim, J.-Y., Qu, J., Jacobs, L., and Viehrig, H.-W., "Evaluation of radiation damage using nonlinear ultrasound," *Journal of Applied Physics*, vol. 111, no. 5, p. 054911, 2012.

[23] McCall, K. and Guyer, R., "Equation of state and wave propagation in hysteretic nonlinear elastic materials," *Journal of Geophysical Research: Solid Earth*, vol. 99, no. B12, pp. 23887–23897, 1994.

[24] Mirzadeh, H. and Najafizadeh, A., "Aging kinetics of 17-4 ph stainless steel," *Materials chemistry and physics*, vol. 116, no. 1, pp. 119–124, 2009.

[25] Murayama, M., Hono, K., and Katayama, Y., "Microstructural evolution in a 17-4 ph stainless steel after aging at 400 c," *Metallurgical and Materials Transactions A*, vol. 30, no. 2, pp. 345–353, 1999.

[26] Nagy, P. B., "Fatigue damage assessment by nonlinear ultrasonic materials characterization," *Ultrasonics*, vol. 36, no. 1, pp. 375–381, 1998.

[27] Odette, G., Lucas, G., and Klingensmith, D., "On the effect of neutron flux and composition on hardening of reactor pressure vessel steels and model alloys," in *MRS Proceedings*, vol. 650, pp. R6–4, Cambridge Univ Press, 2000.

[28] Ostrovsky, L. and Johnson, P., "Dynamic nonlinear elasticity in geomaterials," *Rivista del nuovo cimento*, vol. 24, no. 7, pp. 1–46, 2001.

[29] Payan, C., Garnier, V., Moysan, J., and Johnson, P., "Applying nonlinear resonant ultrasound spectroscopy to improving thermal damage assessment in concrete," *The Journal of the Acoustical Society of America*, vol. 121, no. 4, pp. EL125–EL130, 2007.

[30] Payan, C., Ulrich, T., Le Bas, P., Saleh, T., and Guimaraes, M., "Quantitative linear and nonlinear resonance inspection techniques and analysis for material characterization: Application to concrete thermal damage," *The Journal of the Acoustical Society of America*, vol. 136, no. 2, pp. 537–546, 2014.

[31] Remillieux, M. C., Guyer, R. A., Payan, C., and Ulrich, T., "Decoupling nonclassical nonlinear behavior of elastic wave types," *Physical Review Letters*, vol. 116, no. 11, p. 115501, 2016.

[32] Scruby, C. B. and Drain, L. E., *Laser ultrasonics techniques and applications*. CRC Press, 1990.

[33] Thiele, S., "Air-coupled detection of rayleigh surface waves to assess material nonlinearity due to precipitation in alloy steel," Master's thesis, Georgia Institute of Technology, 2013.

[34] Thiele, S., Kim, J.-Y., Qu, J., and Jacobs, L. J., "Air-coupled detection of nonlinear rayleigh surface waves to assess material nonlinearity," *Ultrasonics*, vol. 54, no. 6, pp. 1470–1475, 2014.

[35] Yost, W. T. and Cantrell, J. H., "The effects of artificial aging of aluminum 2024 on its nonlinearity parameter," in *Review of Progress in Quantitative Nondestructive Evaluation*, pp. 2067–2073, Springer, 1993.